



Trapezoidal Failure Behavior and Fracture Evolution Mechanism of Overburden in Extra-thick Coal Mining in Weakly Cemented Strata

Fangying Dong¹ · Huiyong Yin¹ · Hongxu Ren² · Wenju Cheng² · Shuzhen Tai² · Tianyu Miao² · Yian Zhang³ · Bin Wu⁴

Received: 8 March 2024 / Accepted: 20 August 2024

© The Author(s), under exclusive licence to Springer-Verlag GmbH Austria, part of Springer Nature 2024

Abstract

The abnormal evolution and highly accurate prediction of mining-induced fractures in extra-thick coal play an important role in mine water disaster prevention and ecological environment protection. The evolution mechanism of mining-induced fractures during the mining of extra-thick coal in weakly cemented strata has attracted wide attention. In this paper, the fracture propagation test and PFC numerical simulation are carried out to analyze the evolution rule of overburden fractures in extra-thick coal mining. Based on the elastic foundation beam and fracture damage theory, we derive a trapezoidal fracture model and realize automatic calculation. Finally, taking the 61,605 working face mining of Longwanggou Coal Mine (LWGCM) as an engineering background, the failure characteristics of overburden are studied and verified by microseismic dynamic monitoring. The results show that the overburden failure in mining face is trapezoidal evolution, including shear fractures (93.8%) and tensile fractures (6.2%). The overburden failure height predicted by the trapezoidal fracture model is consistent with the numerical simulation and microseismic monitoring, the relative errors are -1.1% and -2.7% . This provide a new method for the accurate prediction of overburden failure height in extra-thick coal mining in weakly cemented strata.

Highlights

1. Fracture propagation mechanism and simulation of weakly cemented rock.
2. Trapezoidal fracture model and fracture evolution rule of mining overburden.
3. A new method for calculating the overburden failure height of extra-thick coal mining in weakly cemented strata.

Keywords Weakly cemented rock · Fracture propagation · Trapezoidal failure · PFC · Microseismic dynamic monitoring

✉ Huiyong Yin
yhy1919@163.com

Fangying Dong
202082030047@sdust.edu.cn

Hongxu Ren
rhx030822@163.com

Wenju Cheng
202082030045@sdust.edu.cn

Shuzhen Tai
JenssuuTT@163.com

Tianyu Miao
18698756882@163.com

Yian Zhang
2687640078@qq.com

Bin Wu
Wubin1472580369@163.com

- 1 College of Earth Science and Engineering, Shandong University of Science and Technology, Qingdao 266590, Shandong, China
- 2 Shandong Provincial Key Laboratory of Depositional Mineralization and Sedimentary Minerals, Shandong University of Science and Technology, Qingdao 266590, Shandong, China
- 3 Longwanggou Coal Mine, Ordos Guoyuan Mining Development Co., Ltd., Inner Mongolia Zhunger Banner, Ordos 017100, China
- 4 Shanxi Qinxin Coal Industry Co., Ltd., Changzhi 046599, Shanxi, China

Abbreviations

ΣM	Cumulative mining thickness [m]
H_{ew}, H_w, H_{mh}, H_h	Height of overburden failure is extremely weak, weak, medium hard, and hard overburden, respectively [m]
$H_{ij}, H_{mh}, H_{PFC}, H_{mm}$	Height of overburden fracture predicted by trapezoidal fracture model, empirical formula, PFC, and microseismic monitoring, respectively [m]
K_{rat}	Normal-to-shear stiffness ratio [GPa]
E_{mod}	Effective modulus [GPa]
K_n	Normal stiffnesses [GPa]
K_s	Shear stiffnesses [GPa]
P_{b-k_n}	Parallel bonding norma [GPa]
P_{b-k_s}	Parallel bonding shear stiffnesses [GPa]
l_i, l_{i+1}, h_i	Bottom length, top length, height of composite rock layer i , respectively [m]
δ	Fracture extension angle [°]
l'_i	Coal (rock) pillar length [m]
L	Goaf length [m]
q'_{i+1}	Uniform load of composite rock beam [MPa]
q_{i+1}	Uniform load of overburden [MPa]
H	Coal seam depth [m]
H_i	Distance between composite rock beam and coal floor [m]
H	Stress concentration coefficient [-]
$\bar{\rho}_c$	Average density of composite rock beam [kg/m ³]
$\omega_i (l)$	Rock group deflection [m]
$M_i (l)$	Bending moment [KN·m]
$\varphi_i (l)$	Angle [°]
$F_i (l)$	Shear force [N]
E_i	Flexural stiffness [N·m ²]
I	Inertia moment [m ⁴]
k_i	Elastic foundation coefficient [-]
λ	Characteristic coefficient [-]
σ_{imax}	Maximum tensile stress [MPa]
M_{imax}	Maximum bending moment [KN·m]
σ'	Effective stress [MPa]
σ	Non-damage stress [MPa]
$[\bar{\sigma}_i]$	Average tensile strength [MPa]
D	Damage degree [-]
V_1	Volume of mined coal [m ³]
V_2	Volume of rock mass [m ³]
b_1	Width of working face [m]
b_i	Width of composite rock beam [m]

M	Mining thickness [m]
k_p	Expansion coefficient of rock [-]

1 Introduction

Mine water disaster is one of the main hazards to production safety for a long time (Yin et al. 2018). In China, more than 80% mine water disasters are caused by mining-induced fractures connecting water-rich aquifers (Liu et al. 2022; Zhang et al. 2023). The development of ultra-high water-conducting fractures of overburden in extra-thick coal mining has a profound influence on the occurrence and migration of groundwater, which can easily lead to water inrush disaster and ecological environment damage, resulting in property losses and personal casualties (Banerjee et al. 2020; Dong et al. 2024; Liu et al. 2021; Queiroz et al. 2022; Yu et al. 2015). How to accurately predict the height of mining-induced fracture in advance is the key to mine water disaster prevention and control.

Many researchers have studied the failure behavior of mining rock mass and obtained different results (Rezaei et al. 2015; Redondo-Vega et al. 2017). Hasenfus divided the overburden failure into four parts: goaf, highly fractured zone, composite rock beam zone, and surface zone (Hasenfus et al. 1998). Kang proposed that the caving zone is parabolic and the water-conducting fracture zone is saddle-shaped (Kang et al. 2001). Wang suggested that the overall supporting structure of the overburden is a stepped structure of plate shell combination and that the shape of the horizontal section has a rounded rectangle shape (Wang et al. 2019). Liu proposed that the subsidence area of coal seam mining overburden layer is trapezoidal, and puts forward the trapezoidal collapse model, which promotes the research of trapezoidal fracture model of mining overburden (Liu et al. 2022). Meng proposed that the weak bedrock after mining is an asymmetric trapezoidal failure pattern, and the thick loose topsoil shows an inclined funnel-shaped failure pattern (Meng et al. 2023). Cheng monitored the temporal and spatial evolution of overburden deformation during coal mining, revealed the formation, expansion, closure, and reconstructed the fractures (Cheng et al. 2022). Feng studied the rule of rock fracture propagation under different temperature conditions, and revealed ability to fracture toughness and resist fracture propagation of sandstone (Feng et al. 2018). These results have practical significance for understanding the failure characteristics of mining overburden and guiding the safe mining of coal mine.

Coal resources in Eastern China have been mined early. According to a large number of field measured data, some scholars have fitted the formulas (1), (2), (3), and (4) according to the types of coal roof strata combination (extremely weak, weak, medium hard, and hard) (Coal Industry Bureau

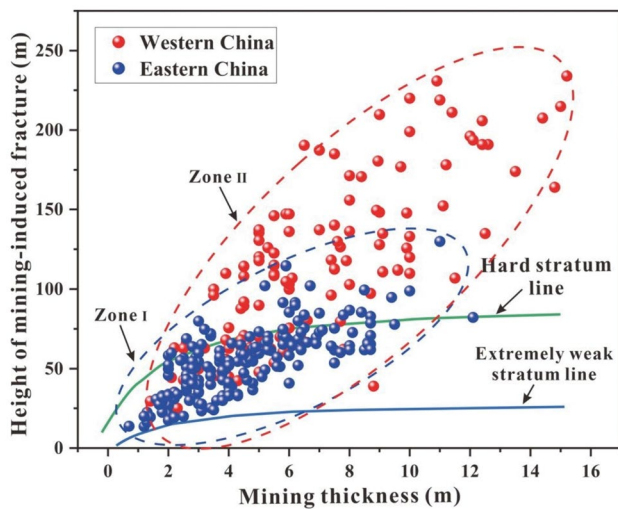


Fig. 1 Comparison of measured height of mining-induced fracture in Eastern and Western China

of China. 2000). However, due to the influence of coal forming environment, the coal-bearing strata are different in the Eastern and Western of China, and the evolution rule of mining-induced fracture in overburden is also different (Dong et al. 2022 a). We collected the measured data of mining-induced fracture height of overburden in the Eastern and Western regions of China, as shown in Fig. 1. When the mining thickness exceeds 4.0 m, the fracture height of mining overburden in the Western region is generally greater than the empirical formula predicted value. In fact, there is still a lack of research on the fracture evolution characteristics of overburden in the mining of extra-thick coal seam in weakly cemented strata in Western China. In the Ordos Basin, the thickness of the Jurassic coal seam is larger, weakly cemented strata are developed, and the mechanical properties of the rock are poor, resulting in the abnormal increase of the development height of mining-induced fracture (Miao et al. 2018). At present, the field measurement methods of mining overburden failure mainly include geophysical monitoring (Su et al. 2017; Wang et al. 2021 b; Wilkins et al. 2020), optical fiber monitoring (Mekhtiev et al. 2022), drilling double-end plugging leak detection, and borehole imaging observation (Stricker et al. 2023). These methods have a good detection in thin coal mining, but the detection of ultra-high mining-induced fractures induced by extra-thick coal mining is often limited (Sun et al. 2019).

$$H_{ew} = \frac{100 \sum M}{5.0 \sum M + 8.0} \pm 3.0 \quad (1)$$

$$H_w = \frac{100 \sum M}{3.1 \sum M + 5.0} \pm 4.0 \quad (2)$$

$$H_{mh} = \frac{100 \sum M}{1.6 \sum M + 3.6} \pm 5.6 \quad (3)$$

$$H_h = \frac{100 \sum M}{1.2 \sum M + 2.0} \pm 8.9 \quad (4)$$

where $\sum M$ is the cumulative mining thickness, m; H_{ew} , H_w , H_{mh} , and H_h are the height of overburden failure when the roof lithology combination is extremely weak, weak, medium hard, and hard, respectively, m.

Numerical simulation is widely used in the study of mining failure characteristics under various conditions, there are still few studies on the fracture development rule of mining overburden by using particle flow code (PFC) (Blixt et al. 2022; Li et al. 2023; Satake et al. 2021; Zhang et al. 2021 b). Liu used PFC to reconstruct a rock's macroscopic structure and microscopic mechanical behavior under uniaxial compression (Liu et al. 2018). Ríos-Bayona constructed a rock shear test model, simulated the peak shear strength of hard crystalline rock, and characterized the shear joint profile and roughness (Ríos-Bayona et al. 2022). Zhang used PFC to study the evolution rule and distribution characteristics of mining-induced fractures and pores in overburden of goaf and proposed the distribution model of circular drum-shaped mining-induced fractures (Zhang et al. 2020). Therefore, using PFC to simulate the evolution of overburden fractures is a practical method. Since mining the Jurassic coal seam in Ordos Basin, many accidents have occurred such as roof water inrush, sand and mud burst (Dong et al. 2022b).

Based on above mentioned, this study takes the mining of extra-thick coal seam in LWGCM as the research object, and comprehensively analyzes the overburden fracture evolution rule of extra-thick coal mining in weakly cemented strata by fracture propagation test, PFC numerical simulation, and microseismic dynamic monitoring. Aim to (1) obtain the fracture propagation rule of weakly cemented rock under uniaxial compression, (2) reveal the trapezoidal evolution characteristics of overburden fracture in extra-thick coal mining, (3) propose a new method for calculating the overburden failure height of extra-thick coal mining in weakly cemented strata.

2 Background and Methods

2.1 Study Area

LWGCM is located in Jungar Coalfield on the Northeast edge of Ordos Basin (Fig. 2). The geographical coordinates are 111° 09' 27" E—111° 16' 57" E, 39° 48' 01" N—39° 50' 45" N. The strata from old to new are Ordovician, Carboniferous, Permian, Triassic, Neogene, and Quaternary strata.

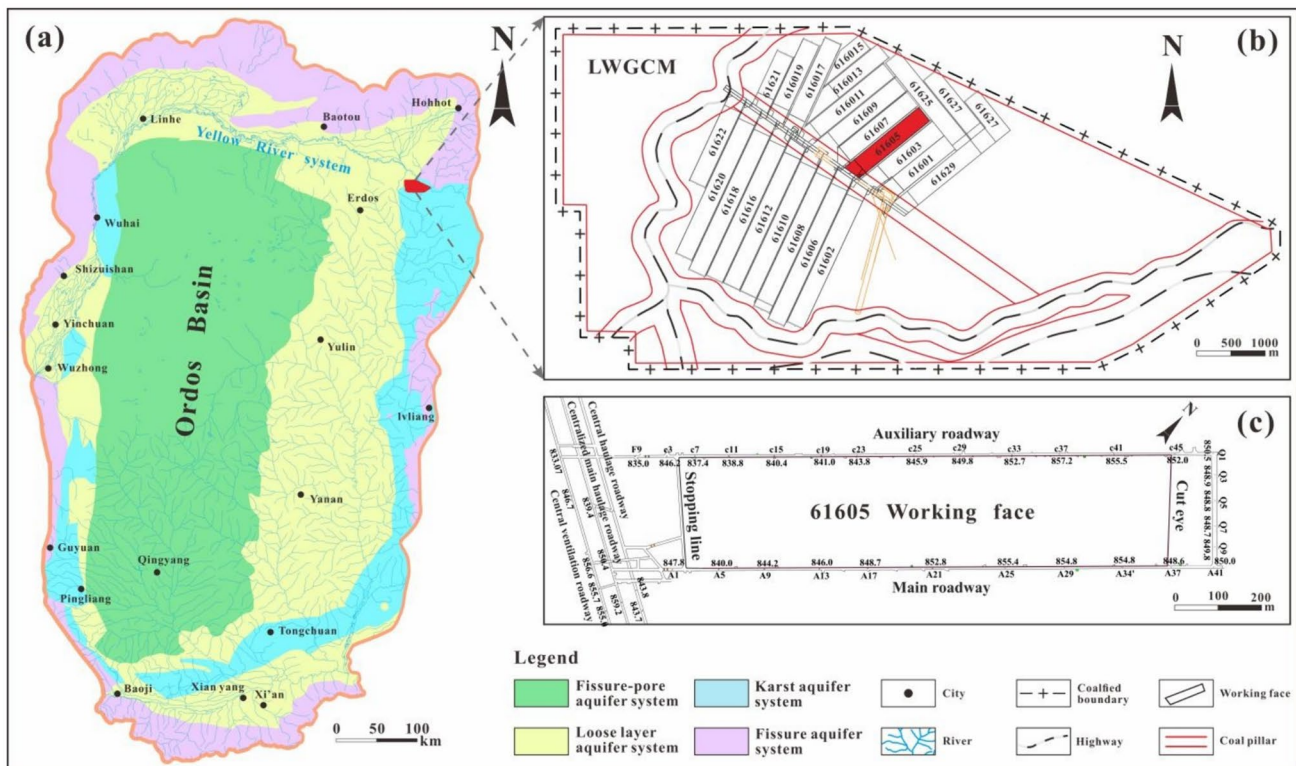


Fig. 2 The location of the study area: a Ordos Basin, b LWGCM, and c 61,605 Working face

The coal-bearing strata are monoclinic structure, strike SN, dip W, and dip angle less than 5°. There are seven layers of coal with an average thickness of 59.47 m and a coal-bearing coefficient of 48.9%. At present, it mainly mining 6rd coal, the average coal thickness is more than 20 m, belongs to extra-thick coal seam.

The coal-bearing strata in the mine belong to weakly cemented strata, which have the characteristics of easy weathering, low strength, and water softening. The lithology is mainly sandstone, containing a small amount of argillaceous rock. The 6rd coal mining different degrees of roof water threats, mainly including thick sandstone water disasters, water and sand inrush disasters, and separated water disasters. The mine adopts the inclined shaft exploit method, fully mechanized top coal caving one-time mining full height process, and the whole caving method manages the roof. The main water filling source is the sandstone aquifer of Shanxi and Shihezi strata. The mining of extra-thick coal seams leads to a high development height of overburden fractures. If the mining-induced fracture connects the strong water-richness aquifers, water inrush will occur. Therefore, based on the mining of 61,605 working face in LWGCM, we study the evolution and development height of mining overburden fractures, which provides a theoretical basis for the prevention and control of roof water disasters in similar mining areas.

2.2 Rock Fracture Propagation

The deformation and failure of overburden under the condition of mining are manifested as rock fracture propagation and penetration on the micro-scale (Deng et al. 2022; Scott et al. 2023; Yang et al. 2022; Zhang et al. 2020). The rock mechanical parameters such as density, porosity, compressive strength, tensile strength, elastic modulus, and Poisson's ratio were obtained by uniaxial compression, brazilian splitting, and porosity test of various rock samples. The simulation test was carried out by PFC software to analyze the fracture propagation and failure evolution rule of rock under uniaxial compression, which provided a basis for the study of fracture development in mining overburden.

The uniaxial compression test was carried out using HCT206A microcomputer controlled oil-electric mixed pressure testing machine, as shown in Fig. 3a. The test equipment is mainly composed of main engine, oil source, and control system. The test machine's digital closed-loop control and measurement system based on a high-speed DSP platform is adopted. The maximum compression space of the test machine is 320 mm, and the displacement resolution is 0.004 mm. The test force error, deformation error, and displacement error are within ±0.5%. The size of rock specimen is Φ 50×100 mm. Displacement control was adopted in the test, and the loading speed was 0.01 mm/min.s

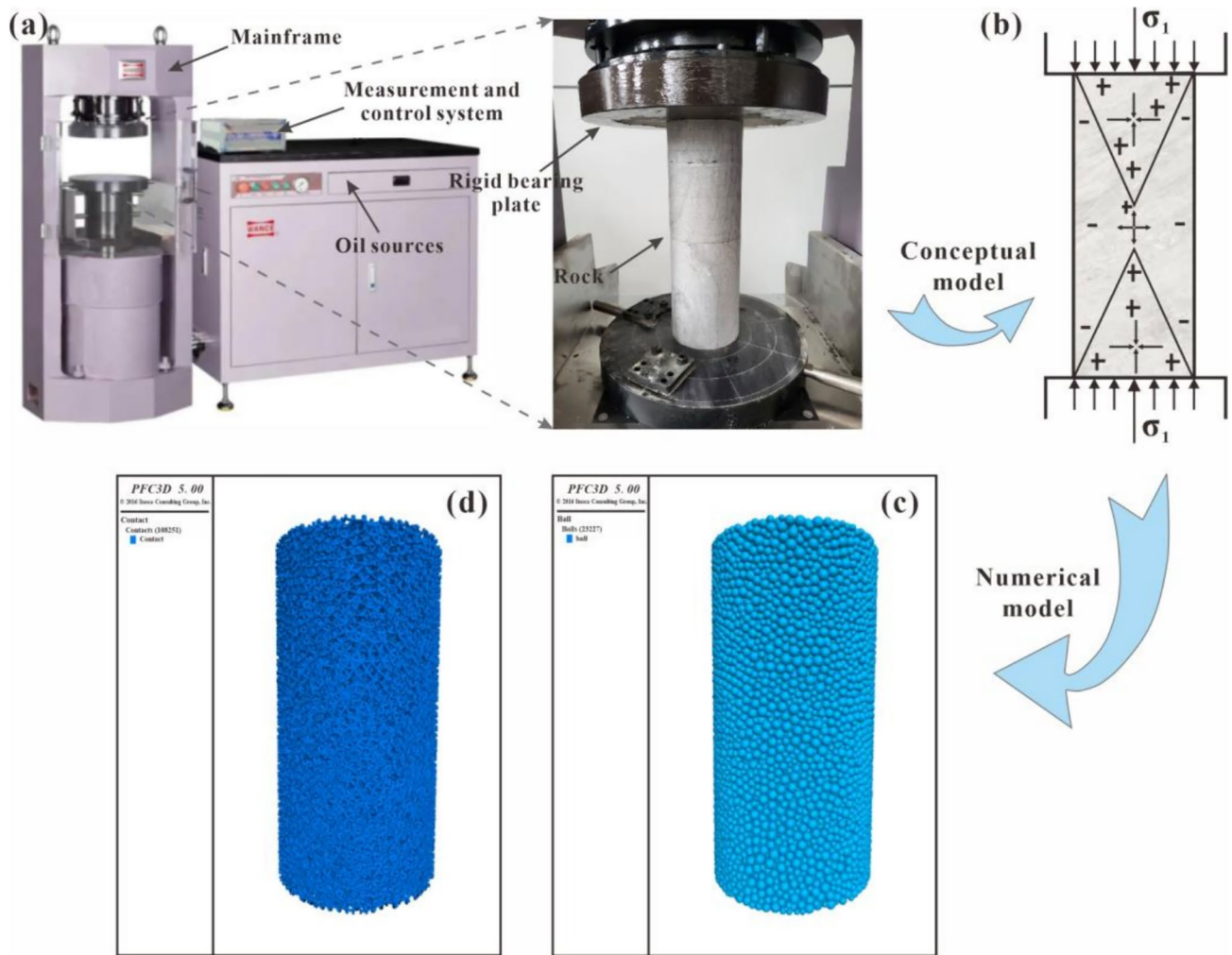


Fig. 3 Uniaxial compression test and PFC numerical model: **a** electro-hydraulic servo pressure testing machine, **b** plane mechanical model diagram of rock, **c** model particle distribution, and **d** model particle contact

Discrete element analysis shows that the deformation and evolution of the whole medium are obtained by the comprehensive description of the displacement and motion state of each discrete individual (Kuva et al. 2012). PFC software bonds independent particle units together to simulate the mechanical behavior of continuous medium materials. Bonding models mainly include contact bonding model (CBM) and parallel bonding model (PBM). The PBM is to bond two particles through a cuboid or disc of a certain thickness. The particle contact model and calculation principle are shown in Fig. 4. PBM can be regarded as a series of springs with normal and tangential stiffness, uniformly distributed on the contact surface of a certain width, which can resist the action of force and moment at the same time. Therefore, this paper chooses PBM to simulate the fracture propagation behavior during rock failure. According to the uniaxial compression test, the conceptual model is constructed (Fig. 3b). The PFC software is used to construct the numerical model, and the

mesoscopic parameters are shown in Table 1. A particle system was created, and a total of 23,227 particles (Fig. 3c) and 108,251 contact points (Fig. 3d) were generated in the model, all compressive contacts.

2.3 Trapezoidal Fracture Evolution Model

Scholars in related fields have studied many similar material simulation experiments under different conditions of coal seam excavation (Cai et al. 2020; Liu et al. 2020; Zhang et al. 2021a). Figure 5 shows similar materials' simulation results in Shilawusu and Yingpanhao coal mine. Two coal mine are located in the Ordos Basin, belonging to weakly cemented coal-bearing strata, and full-mechanized caving of coal seams, with similar geological conditions in the study area. In Shilawusu coal mine, the simulated mining thickness is 9 m, the mining depth is 650 m. After mining, the height of the mining-induced fracture zone is 196 m, and the fracture mining ratio is 21.78.

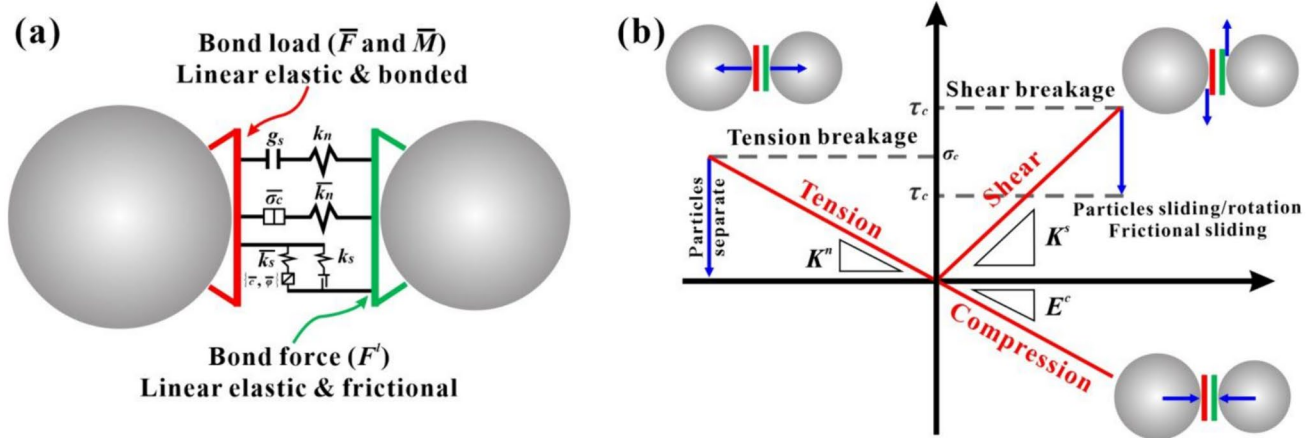


Fig. 4 PFC particle contact model and calculation principle: a parallel bond model, and b bonding deformation and calculation principle

Table 1 Micro-parameters of uniaxial compression simulation

Parameters	Parameters	Parameters	Parameters
R_{max}	6×10^{-3} m	p_{b_mul}	0.6
R_{min}	3×10^{-3} m	$p_{b_k_{rat}}$	1.5
dens	2.5×10^3 kg/m ³	p_{b_emod}	1.86×10^3 MPa
fric	0.1	p_{b_ten}	17.2 MPa
porosity	0.2	p_{b_coh}	6.37 MPa

While, in Yingpanhao coal mine, the simulated mining thickness is 5.5 m and the mining depth is 550 m (Fig. 5a). After mining, the height of the mining-induced fracture zone is 115.5 m and the fracture mining ratio is 21 (Fig. 5b). The results show that the fracture of overburden is similar to the trapezoid with a wide bottom and narrow top in thick coal seam mining in weakly cemented strata. Based on this, we generalize the development process of mining-induced fracture in different excavation stages as Fig. 6. During the excavation of the coal mining, the immediate roof is deformation, bending, and cracking under the action of stress, resulting in an inverted “V” fractures (Fig. 6a). When the length of the overhanging roof is greater than the limit span

of the rock layer, the immediate roof will caving (Fig. 6b). After the immediate roof caving, the basic roof is in a suspended state, breaking the stress equilibrium state. The basic roof bents under the combined action of overburden gravity and horizontal tectonic stress (Fig. 6c). With the mining of the working face, the basic suspended area of the roof increases, cracking, and caving gradually (Fig. 6d and Fig. 6e). Based on the trapezoidal failure of overburden and the rule of rock expansion, we propose a new method for calculating the overburden failure height.

2.4 PFC Numerical Simulation

Taking 61,605 mining face of LWGCM as the background, the particle flow discrete element geological model is constructed using PFC software (Fig. 7a and b). The strata in the working face are generalized and divided into 31 layers (Fig. 7c). The size of the model is 600×450 m, the number of randomly generate particles are 130,677, and the contact points are 293,929. The initial displacement and stress are cleared after the rock layer is added gravity. There are 100 m protective coal (rock) pillars on both sides of the model. The length of the simulated excavation is 400 m, and the mining thickness is 23 m. Eight displacement measuring lines are arranged longitudinally on the coal seam roof, with a spacing of 40 m. Displacement measuring points are arranged every 20 m on the transverse, and 120 measuring points are arranged. Four stress measuring lines are arranged in the longitudinal direction, with a spacing of 75 m. Stress measuring points are arranged every 25 m in the transverse, and 68 measuring points are arranged (Fig. 7d). To select accurate macro and micro mechanical parameters, we use PFC software to calibrate the mechanical parameters of the particles. At the same time, the microscopic parameters of each rock layer are corrected by an orthogonal test, primary effect analysis, and regression fitting method (Huang et al.

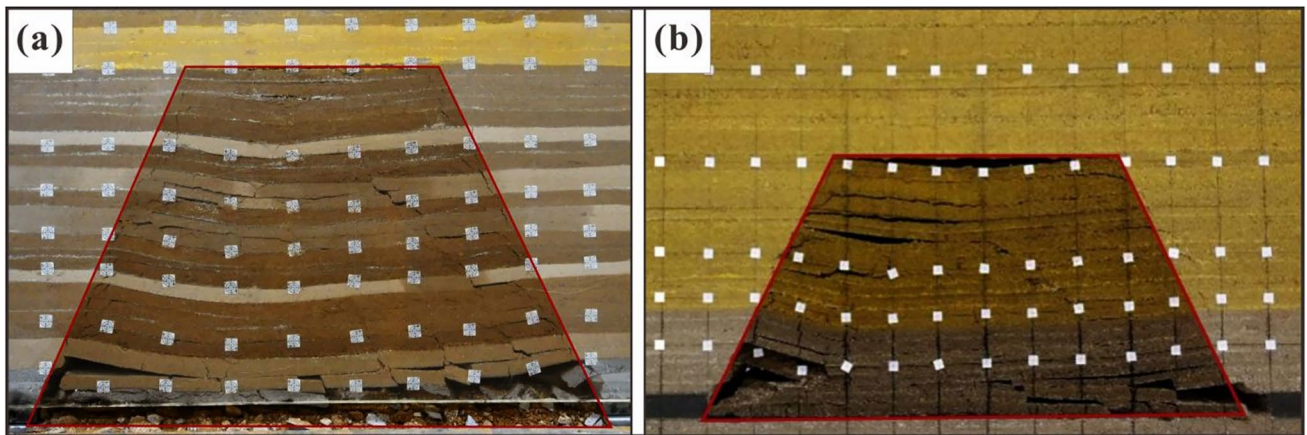


Fig. 5 Failure characteristics of mining overburden by similar materials simulate: **a** Shilawusu Coal Mine, and **b** Yingpanhao Coal Mine

2021). The macro and micro mechanical parameters of each stratum are shown in Table 2.

2.5 Microseismic Dynamic Monitoring

The KJ551 microseismic monitoring system is used in LWGCM to monitor the 61,605 working face mining. Twelve geophones are arranged in the main and auxiliary roadway. The distance between the geophones is 100 m. Four roof geophones and two floor geophones are installed in every roadway, the cross arrangement of roof and floor is adopted. When the mining to 20 m from the geophone, withdrawn the geophone and installed backward to ensure more than four geophones are monitored the same microseismic event. The microseismic monitoring system of working face is shown in Fig. 8.

3 Results and Discussions

3.1 Rock Mechanical Properties and Fracture Propagation Mechanism

3.1.1 Mechanical Properties

There are 456 groups of rock samples collected from coal-bearing strata of LWGCM, and rock mechanics tests were carried out. The mechanical parameters of coarse sandstone, fine sandstone, sandy mudstone, and coal are shown in Table 3. Generally, the uniaxial compressive strength, tensile strength, and cohesion of coarse sandstone and sandy mudstone are larger, indicating that the mechanical properties of rock are better. The variation characteristics of parameters (compressive strength, tensile strength, cohesion, internal friction angle, elastic modulus, Poisson's ratio, density, and porosity) with buried depth are shown in Fig. 9. It can be seen that the mechanical parameters of same lithology have

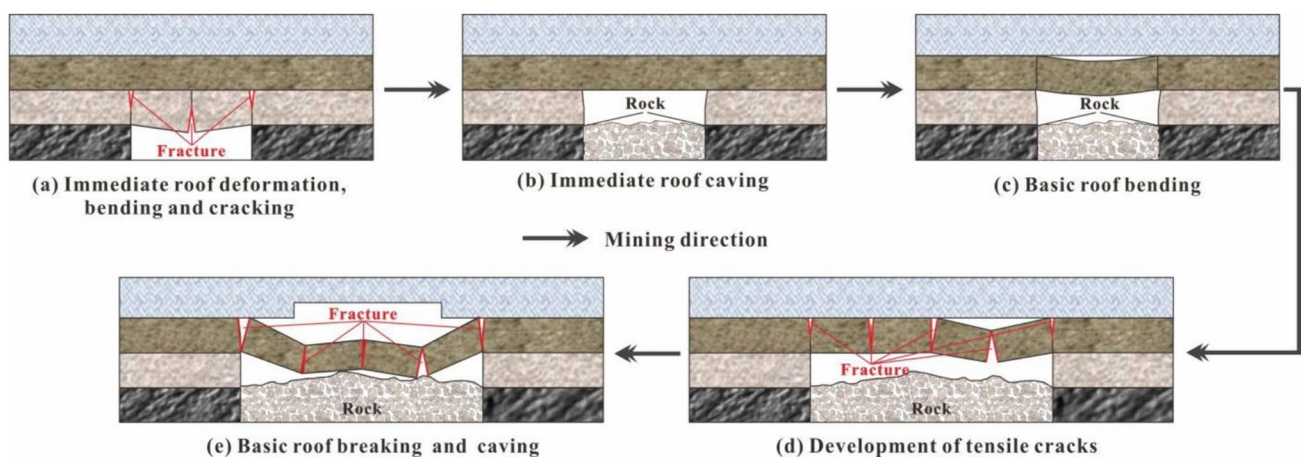


Fig. 6 Failure evolution model of overburden in coal mining (revised from Liu et al. 2022)

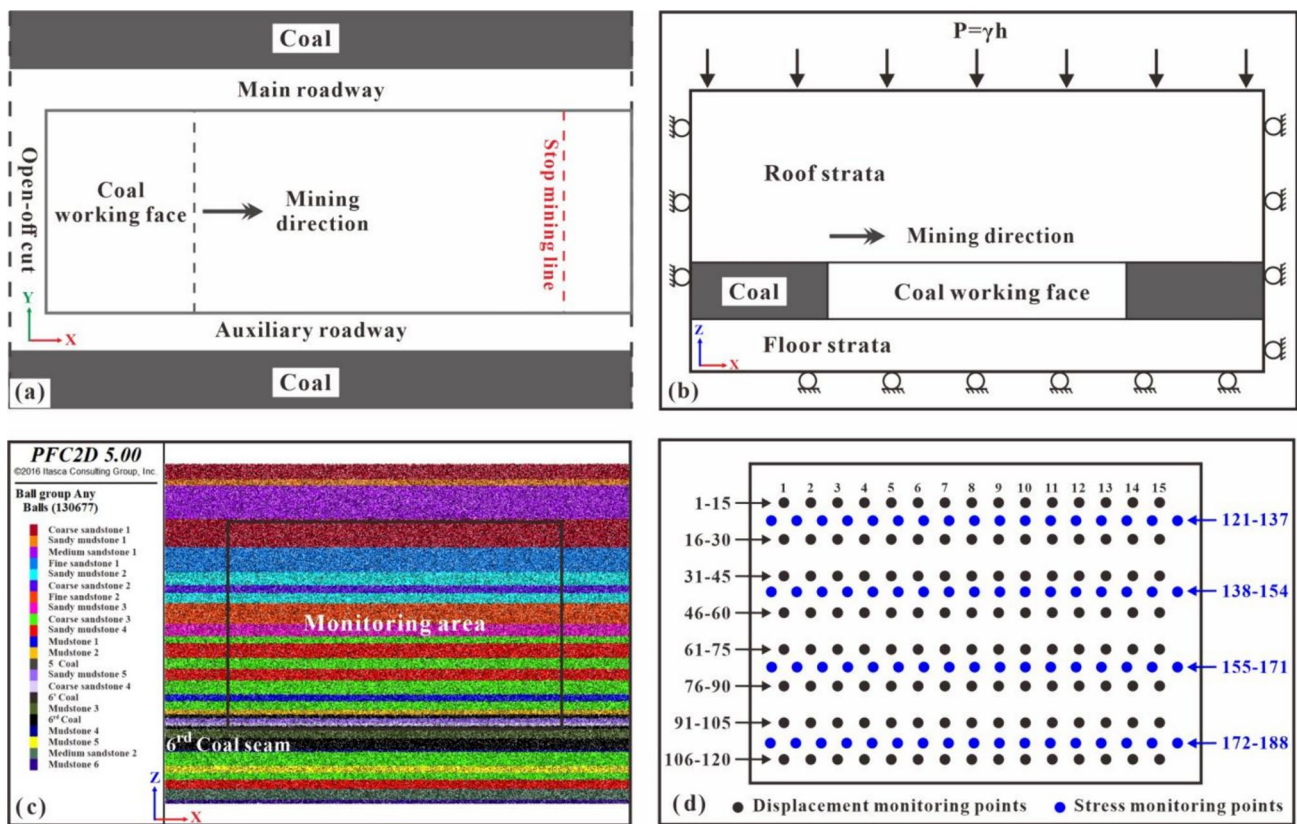


Fig. 7 Theoretical model and simulation model: **a** plane model, **b** profile model, **c** numerical analysis model, and **d** location distribution of monitoring points

an increasing trend with buried depth. The uniaxial compressive strength, tensile strength, and density increase most obvious.

3.1.2 Fracture Propagation Rules and Parameter Calibration

The development of mining-induced overburden fractures are caused by the propagation and penetration of micro-fractures in the rock. Through the uniaxial compression test, the generation, propagation, and penetration of micro-fractures are observed during the failure of coal (rock). The experimental process was generalized into a PFC numerical model to simulate the evolution rule of contact force, fracture state (tensile fracture and shear fracture), fracture number and direction during uniaxial compression. Moreover, the mechanical parameters of the particles are calibrated according to the compressive strength, Poisson's ratio, and elastic modulus obtained by uniaxial compression test, including effective modulus, stiffness ratio, meso tensile strength, and meso cohesion. The effective modulus determines the macroscopic elastic modulus of the rock. The stiffness ratio determines the macroscopic Poisson's ratio of the rock. The

ratio of meso tensile strength to meso cohesion determines the failure mode of rocks, and the size of ratio determines the compressive strength.

Figure 10 shows the failure behavior during uniaxial compression and the development of fractures at different stages in PFC numerical model. The process of failure are divided into pore compaction (Fig. 10a), initial fracture (Fig. 10b), elastic stage (Fig. 10c), peak moment (Fig. 10d), and post-peak stage (Fig. 10e). The numerical analysis of the fracture development morphology in the post-peak stage is consistent with the uniaxial compression (Fig. 10f). The stress–strain–fracture variation curve can be divided into four stages (Fig. 11): (1) No fracture stage (I). The rock is in the compaction stage, with no fractures generated; (2) Micro-fracture propagation stage (II). There are small number of micro-fractures are generated in the rock, and the fractures increases linearly, including initial fracture stage and elastic stage. There are 1184 micro-fractures are generated, including 14 tensile fractures and 1170 shear fractures. The tensile fracture are mainly distributed at both ends of the specimen, while the shear fracture evenly distributed inside the specimen; (3) Micro-fracture accelerated propagation stage (III). Before the peak stage, many micro-fractures developed, and

Table 2 The macro and micro mechanical parameters of rock layers in PFC model

Stratum	Lithology	Thickness (m)	Macroscopic parameters				Mesoscopic parameters							
			Density	Poisson's ratio	Elastic modulus (GPa)	Compressive strength (MPa)	Cohesion (MPa)	Internal friction angle (°)	K_{rat} (GPa)	E_{mod} (GPa)	K_n (GPa)	K_s (GPa)	P_{b-k_n} (GPa)	P_{b-k_s} (GPa)
J1	Coarse sandstone 1	30.00	2557	0.24	2.26	16.80	2.9	43.02	1.26	4.80	32.86	26.08	13.47	10.69
J2	Sandy mudstone 1	8.28	2292	0.15	2.82	12.40	6.1	32.00	1.65	3.26	34.26	20.76	18.69	11.33
J3	Medium sandstone 1	42.72	2628	0.29	2.11	12.80	6.8	36.00	1.30	3.60	23.11	17.78	14.45	11.12
J4	Coarse sandstone 1	37.43	2557	0.24	2.26	16.80	2.9	43.02	1.26	4.80	32.86	26.08	13.47	10.69
J5	Fine sandstone 1	31.60	2620	0.13	2.08	9.90	5.9	34.20	1.30	6.40	28.47	21.90	15.64	12.03
J6	Sandy mudstone 2	17.11	2403	0.19	2.45	32.72	6.2	36.17	1.83	4.26	34.67	18.95	21.42	11.70
J7	Coarse sandstone 2	10.00	2361	0.27	4.69	38.60	5.6	37.02	1.95	8.74	40.49	20.76	25.31	12.98
J8	Sandy mudstone 2	17.11	2403	0.19	2.45	32.72	6.2	36.17	1.83	4.26	34.67	18.95	21.42	11.70
J9	Fine sandstone 2	27.42	2588	0.20	2.17	17.17	7.2	33.10	1.64	6.70	33.86	20.65	21.16	12.90
J10	Sandy mudstone 3	15.60	2468	0.20	3.03	19.23	7.2	37.50	1.77	4.52	33.28	18.80	16.57	9.36
J11	Coarse sandstone 3	8.78	2600	0.25	2.71	20.97	3.6	34.28	1.60	5.80	36.52	22.83	16.46	10.29
J12	Sandy mudstone 4	19.22	2499	0.22	3.61	24.62	7.8	38.43	1.68	4.24	34.77	20.70	17.24	10.26
J13	Coarse sandstone 3	13.62	2600	0.25	2.71	20.97	3.6	34.28	1.60	5.80	36.52	22.83	16.46	10.29
J14	Sandy mudstone 4	19.22	2499	0.22	3.61	24.62	7.8	38.43	1.68	4.24	34.77	20.70	17.24	10.26
J15	Coarse sandstone 3	17.52	2600	0.25	2.71	20.97	3.6	34.28	1.60	5.80	36.52	22.83	16.46	10.29
J16	Mudstone 1	8.80	2660	0.17	3.25	23.87	3.8	31.00	1.97	2.26	22.23	11.28	10.86	5.51
J17	Coarse sandstone 3	11.40	2600	0.25	2.71	20.97	3.6	34.28	1.60	5.80	36.52	22.83	16.46	10.29
J18	Mudstone 2	6.20	2660	0.12	2.45	19.58	3.8	31.00	1.80	2.24	23.11	12.84	12.63	7.02
J19	5 Coal	2.50	2256	0.12	2.51	5.80	3.8	37.18	1.77	1.63	3.25	1.84	2.03	1.15
J20	Sandy mudstone 5	5.60	2504	0.26	3.27	28.00	5.5	35.52	1.78	3.82	38.21	21.47	17.89	10.05
J21	Coarse sandstone 4	3.65	2581	0.26	2.90	20.60	3.4	36.31	1.84	6.56	38.26	20.79	18.75	10.19
J22	6 [#] Coal	3.75	2336	0.14	2.70	4.50	3.4	35.87	1.61	2.59	5.17	3.21	3.23	2.01
J23	Mudstone 3	4.35	2660	0.19	2.64	19.47	4.8	31.00	1.80	4.78	24.12	13.40	13.56	7.53
J24	6rd Coal	23.10	2576	0.15	2.22	8.10	4.4	35.63	2.04	2.80	5.60	2.75	3.50	1.72
J25	Mudstone 4	3.40	2361	0.23	2.60	12.49	7.2	36.00	1.56	6.60	20.58	13.19	11.23	7.20
J26	Coarse sandstone 3	17.86	2600	0.25	2.71	20.97	3.6	34.28	1.60	5.80	36.52	22.83	16.46	10.29
J27	Mudstone 5	8.77	2671	0.28	1.40	12.80	6.5	30.92	1.77	2.53	24.56	13.88	12.53	7.08
J28	Coarse sandstone 3	8.75	2600	0.25	2.71	20.97	3.6	34.28	1.60	5.80	36.52	22.83	16.46	10.29
J29	Sandy mudstone 4	19.22	2499	0.22	3.61	24.62	7.8	38.43	1.68	4.24	34.77	20.70	17.24	10.26
J30	Medium sandstone 2	13.60	2647	0.28	7.70	17.68	4.4	36.25	1.56	6.60	25.13	16.11	12.67	8.12
J31	Mudstone 6	5.50	2814	0.34	3.12	18.20	8.3	32.14	1.77	3.24	22.63	12.79	11.34	6.41

K_{rat} is the normal-to-shear stiffness ratio, GPa; E_{mod} is the effective modulus, GPa; K_n is the normal stiffnesses, GPa; K_s is the shear stiffnesses, GPa; P_{b-k_n} and P_{b-k_s} are the parallel bonding normal and parallel bonding shear stiffnesses, respectively, GPa

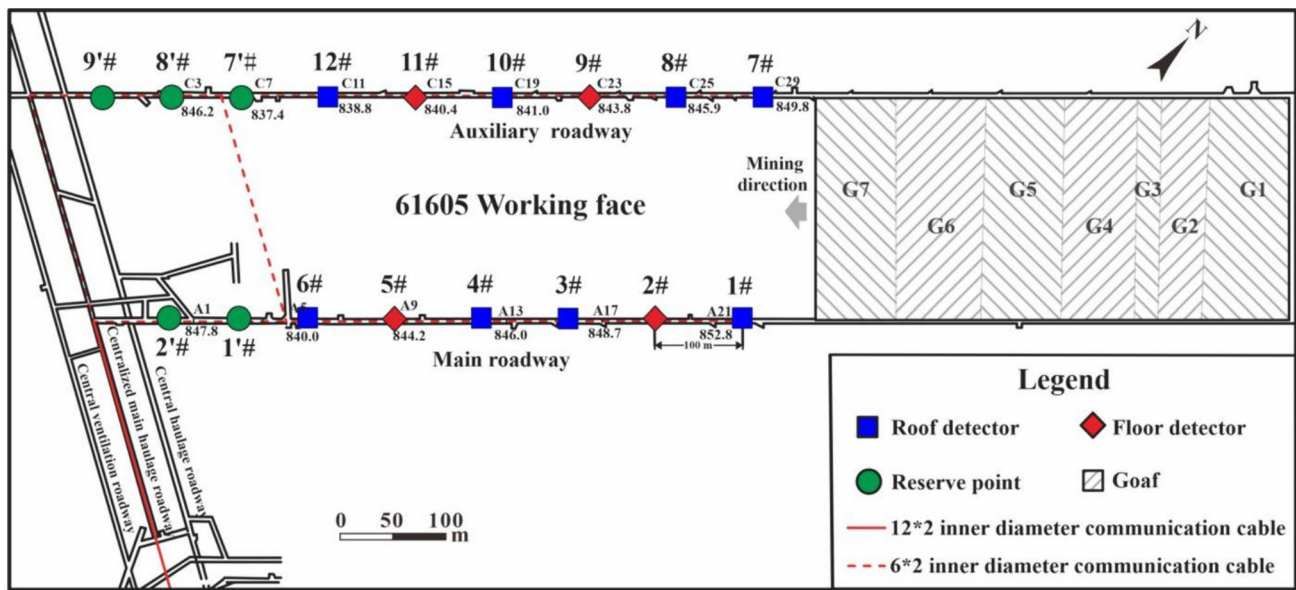


Fig. 8 Microseismic monitoring system of 61,605 Working face in LWGCM

Table 3 Rock mechanics parameters of LWGMC

	Coarse sandstone		Fine sandstone		Sandy mudstone		Coal	
	Range	Median	Range	Median	Range	Median	Range	Median
Compressive strength (MPa)	2.70–52.50	15.42	3.03–47.70	9.19	1.23–53.80	14.55	2.40–53.80	6.20
Tensile strength (MPa)	0.10–9.78	1.03	0.10–4.21	0.93	0.10–5.51	1.14	0.20–0.94	0.62
Cohesion (MPa)	0.30–17.50	3.70	0.20–12.30	2.95	0.50–14.60	4.80	0.50–7.30	4.40
Internal friction angle (°)	32.35–43.02	37.04	23.17–43.02	37.48	25.98–38.72	35.65	34.12–38.72	36.28
Elastic modulus (GPa)	0.53–4.69	1.24	0.38–7.94	2.17	0.45–4.44	2.49	2.03–3.81	2.51
Poisson's ratio	0.08–0.76	0.23	0.06–0.42	0.19	0.08–0.63	0.23	0.08–0.42	0.18
Density (kg/m ³)	2359–2938	2643	2492–2770	2647	2143–2992	2643	2256–2830	2576
porosity (%)	1.90–36.23	16.66	0.39–34.83	15.61	0.20–29.83	9.40	4.57–12.40	7.81

the number of fractures increased nonlinearly. Many microfractures developed and tended to be connected, resulting in 3151 microfractures, including 27 tensile fractures and 3124 shear fractures; (4) Post-peak fractures coalescence failure stage (IV). The microfractures inside the specimen expand rapidly, the microfractures are connected, and the macroscopic fracture surface appears. A total of 34,194 microfractures are generated when the specimen is failed, including 2021 tensile fractures and 32,173 shear fractures. The number of fractures after the peak point accounts for about 94% of the total fractures in the whole failure process. It can be seen from Table 4 and Fig. 11 that the relative errors of peak stress, elastic modulus, and Poisson's

ratio between experimental and simulated results are 0.06%, 1.46%, and 0.0%, respectively. PFC simulation results can effectively characterize the deformation and failure process of rock.

In fact, the generation and propagation of fractures in rocks are closely related to the ability of rock materials to resist failure (Feng et al. 2018, 2020; Wang et al. 2019). According to the failure morphology and fractures development of specimens at different stages (Fig. 10), fractures first occur in the stress concentration area, resulting in tensile fractures. The internal fractures of the specimen continue to expand before the peak point, showing a trend of more at both ends and less in the middle, and some fractures penetration. After the peak point, the fractures

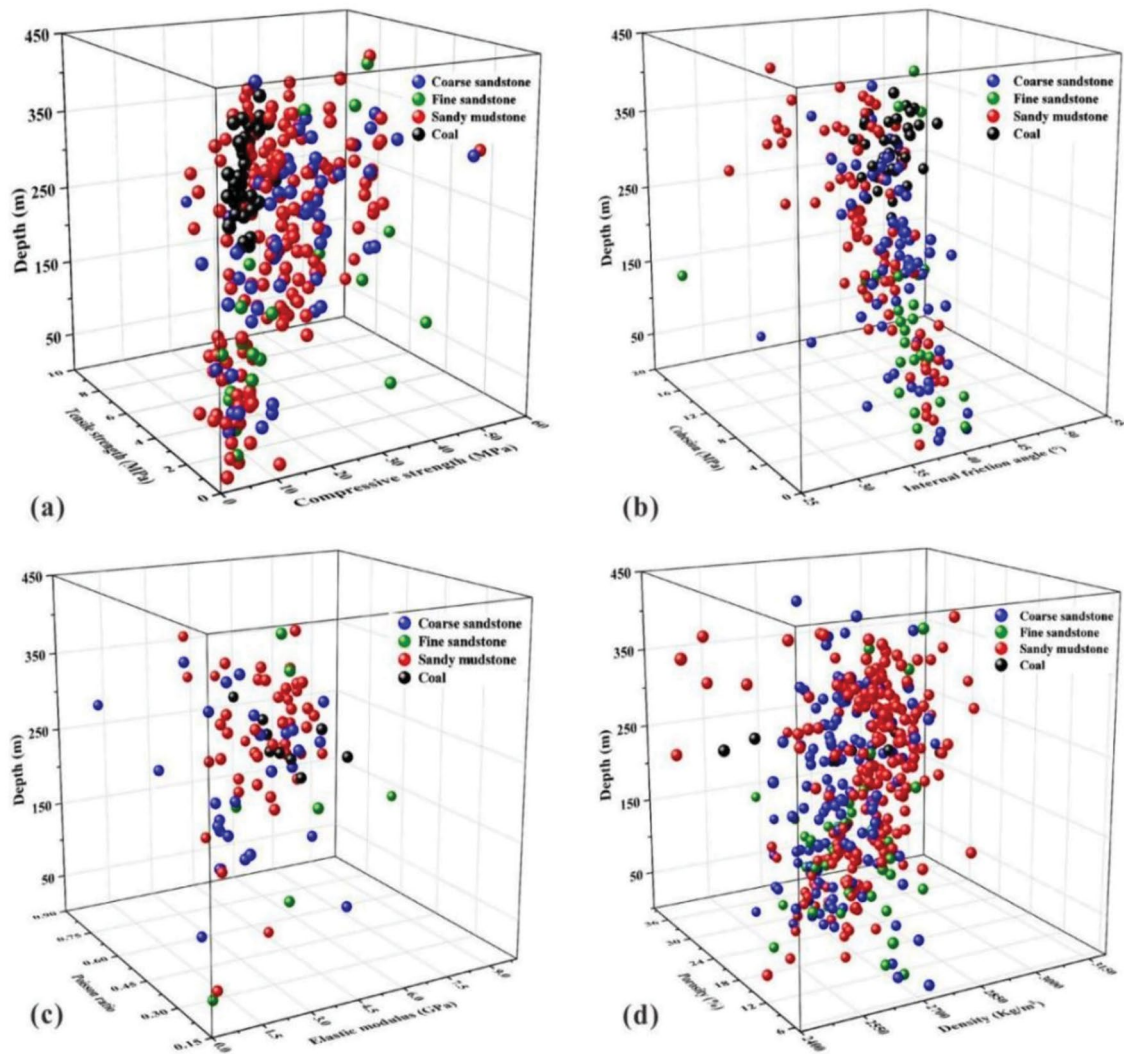


Fig. 9 The 3D intersection diagram of mechanical properties of coal (rock) strata: **a** compressive and tensile strength, **b** internal friction angle and cohesion, **c** elastic modulus and Poisson’s ratio, and **d** density and porosity

developed rapidly from both ends to the middle, and the fracture development rate reached the peak value until the specimen is a failure. The specimen does not suddenly failure at the peak point but the micro-fractures accelerate development and penetration (Fig. 11). When the micro-fractures converge to form a complete fracture surface, the rock specimen suddenly failure.

3.2 Calculation of Overburden Failure Height Based on Trapezoidal Fracture Model

3.2.1 Model Derive

Figure 12 is the schematic diagram of trapezoidal fracture model of overburden. The model is divided into n composite

rock beams. According to the geometric relationship of the composite rock beam of the layer i :

$$l_{i+1} = l_i - 2 \frac{h_i}{\tan \delta} \tag{5}$$

$$l'_i = \frac{L - l_i}{2} \tag{6}$$

where l_i , l_{i+1} , h_i are the bottom length, top length, height of composite rock layer i , respectively, m; l'_i is the corresponding coal (rock) pillar length, m; L is the goaf length, m; δ is the fracture extension angle of the roof strata, °. The δ can be obtained by actual measurement after mining, while it is generally obtained by similar material simulation, numerical simulation, or empirical value before mining. This paper

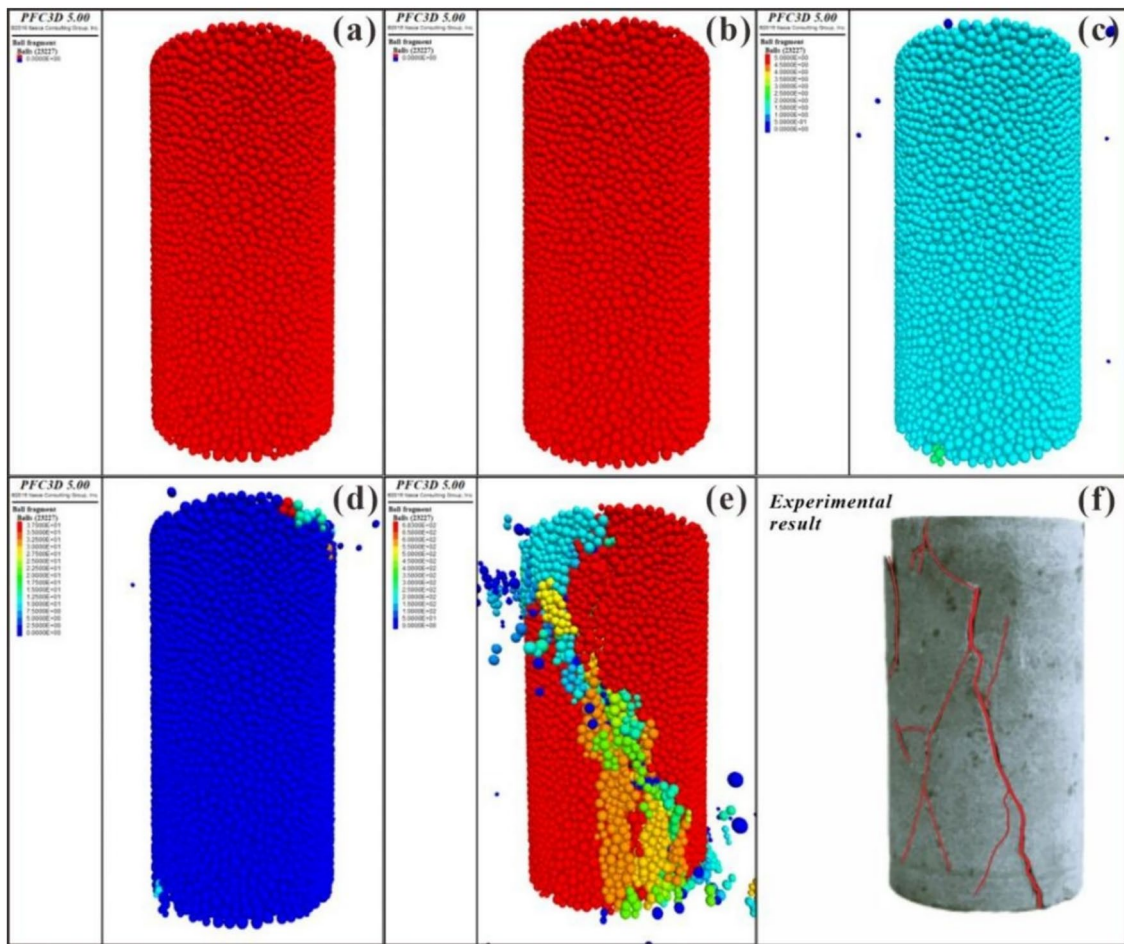


Fig. 10 The failure behavior and fracture development in different stages: **a** pore compaction, **b** initial fracture, **c** elastic stage, **d** peak time, **e** post-peak stage, and **f** experimental result

Fig. 11 The stress–strain–fracture variation curve of the experimental and simulated

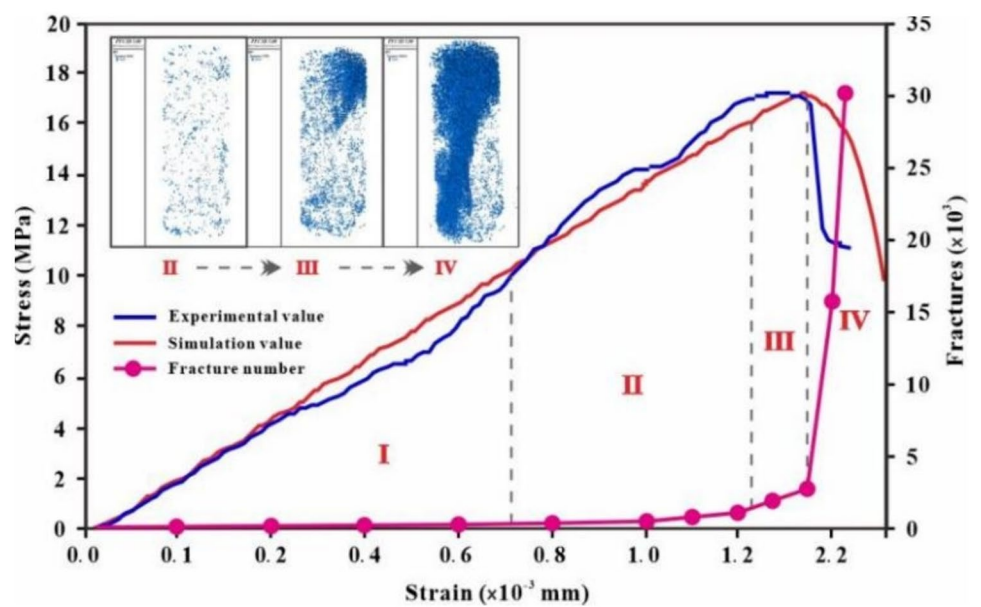


Table 4 Comparison of simulation values with experimental values

	Peak stress (MPa)	Elastic modulus (MPa)	Poisson's ratio
Experimental results	17.18	1370	0.25
Simulation results	17.17	1350	0.25
Relative error (%)	0.06	1.46	0.0

mainly adopts numerical simulation to obtain the value is 65°.

The stress above the coal (rock) pillar of the layer *i* composite rock beam, simplified as a uniform load, q_{i+1}' is the gravity of the overburden. The Eq. 7 as follows:

$$q'_{i+1} = \eta \bar{\rho}_c g (H - H_i) \tag{7}$$

where q_{i+1}' is the uniform load of composite rock beam, MPa; H is the coal seam depth, m; H_i is the distance between composite rock beam and coal floor, m. η is the stress concentration coefficient above the coal (rock) pillar; $\bar{\rho}_c$ is the average density of composite rock beam, kg/m³.

When the coal (rock) pillar is deformed and failed, the subsidence deflection is generated locally in the overburden. According to E. Winkler's elastic foundation theory (Chauhan et al. 2023; Zhang et al. 2022), the deflection of the rock group above the coal (rock) pillar of the layer *i* composite rock beam can be calculated by Eq. 8.

$$E_i I \frac{d^4 \omega_i(l)}{dl_i^4} + k_i \omega_i(l) = \eta \bar{\rho}_c g (H - H_i) \tag{8}$$

where $\omega_i(l)$ is the deflection of the rock group; E_i is the flexural stiffness, N·m²; I is the moment of inertia, m⁴; k_i is the elastic foundation coefficient, $k_i = E_i/h_i$.

According to Eq. 7 and Eq. 8, the general solution of the deflection equation of the layer *i* rock beam in the range of $0 \leq l \leq l'_i$ can be obtained as follows:

$$\omega_i(l) = e^{\lambda l} (A_1 \cos \lambda l_i + B_1 \sin \lambda l_i) + e^{-\lambda l} (C_1 \cos \lambda l_i + D_1 \sin \lambda l_i) + \frac{\eta \bar{\rho}_c g (H - H_i)}{k_i} \tag{9}$$

where λ is the characteristic coefficient, $\lambda = \sqrt[4]{k_i b / 4 E_i I}$; A_1 , B_1 , C_1 , and D_1 are the constants.

The goaf formed after coal mining makes overburden in a suspended state. The uniform load q_{i+1} on the composite rock beam of layer *i* of overburden is calculated by Eq. 10:

$$q_{i+1} = \bar{\rho}_c g (H - H_i) \tag{10}$$

where q_{i+1} is the uniform load of overburden, MPa.

Both sides of the boundary coal (rock) pillar are set as fixed boundaries, and the composite rock beam of overburden can be regarded as a fixed beam. The deflection equation of the layer *i* composite rock beam in the range of $l'_i \leq l \leq l_i/2$ as follows:

$$E_i I \frac{d^4 \omega_i(l)}{dl_i^4} = \bar{\rho}_c g (H - H_i) \tag{11}$$

According to Eq. 10 and Eq. 11, the general solution of the deflection equation of the composite rock beam in the range of $l'_i \leq l \leq l_i/2$ as follows:

$$\omega_i(l) = \frac{\bar{\rho}_c g (H - H_i) l_i^4}{24 E I} + \frac{A_2 l_i^3}{6} + \frac{B_2 l_i^2}{2} + C_2 l_i + D_2 \tag{12}$$

where A_2 , B_2 , C_2 , and D_2 are constants.

According to the trapezoidal beam model structure and load symmetrical distribution characteristics, the deflection $\omega_i(l)$, bending moment $M_i(l)$, angle $\phi_i(l)$, and shear force $F_i(l)$ are equal at the symmetric position of the composite rock beam. When $\omega \rightarrow 0$, $\phi \rightarrow 0$, the boundary conditions of the composite rock beam of layer *i* are as follows:

$$\begin{cases} \phi_i(l = l_i) = 0 \\ F_i(l = l_i) = 0 \\ \omega_i(l = l_i) = 0 \\ \phi_i(l = l_i + l'_i) = 0 \\ \omega_i(l = l_i + l'_i) = 0 \end{cases} \tag{13}$$

According to E. Winkler's elastic foundation theory, the relationship between $\omega_i(l)$, $\phi_i(l)$, $F_i(l)$, and $M_i(l)$ of composite rock beams as follows:

$$\begin{cases} M_i(l) = -EI \frac{d\omega^2(l)}{dl^2} \\ F_i(l) = -EI \frac{d\omega^3(l)}{dl^3} \\ \phi_i(l) = \frac{d\omega(l)}{dl} \end{cases} \tag{14}$$

According to the theory of maximum tensile stress (Li et al. 2019; Wang et al. 2021a; Zhu et al. 2023), when the maximum tensile stress of the material exceeds its ultimate value, the material failure. The maximum tensile stress of the composite rock beams can be obtained by Eq. 15 based on the theory of rectangular section beam (Zhang et al. 2022).

$$\sigma_{imax} = \left| \frac{6M_{i\max}}{h_i^2} \right| \tag{15}$$

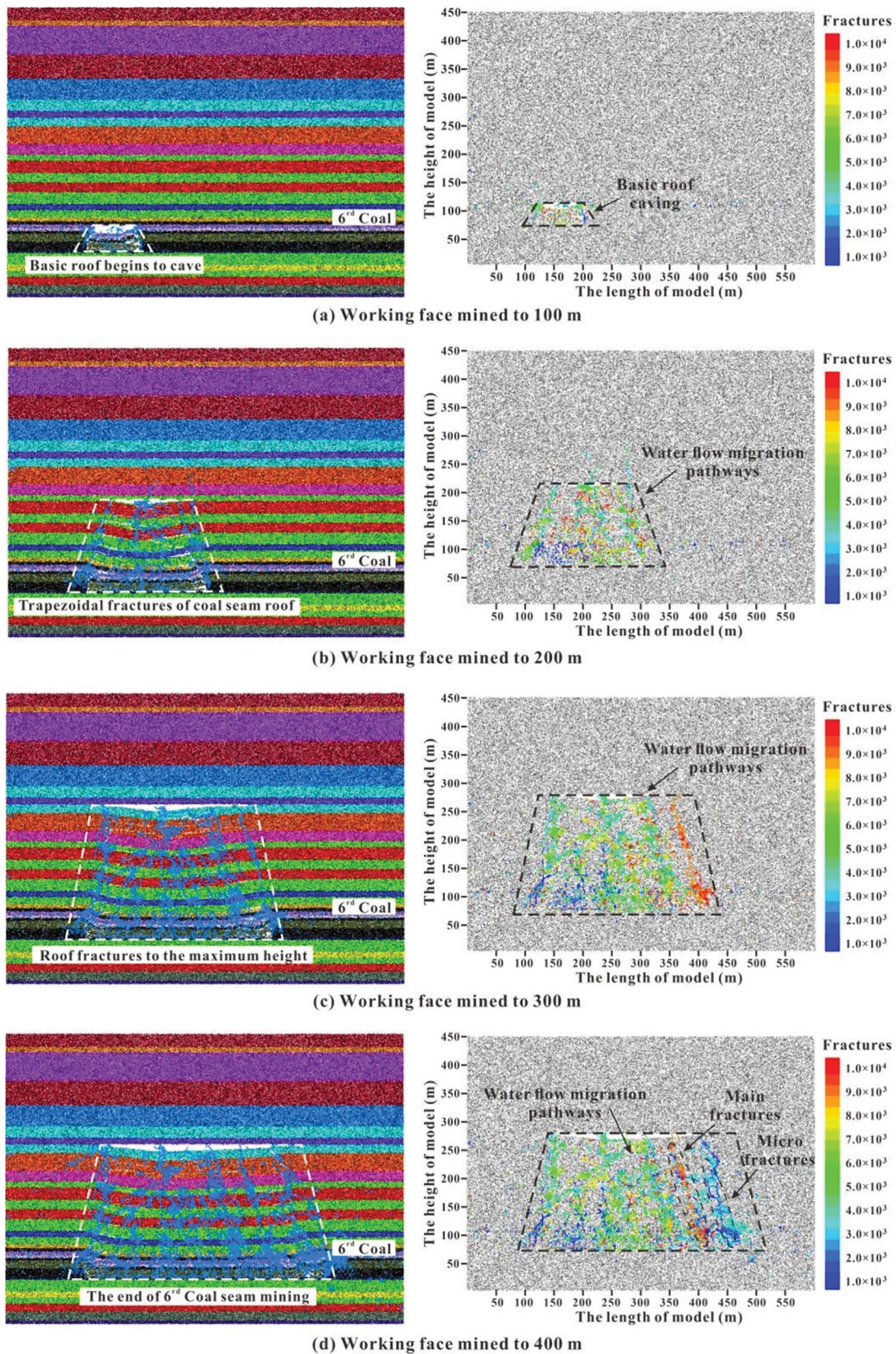


Fig. 12 Mining-induced fracture evolution of overburden in working face

where σ_{imax} is the maximum tensile stress of the composite rock beam, taking the weighted average tensile stress of the rock strata inside the composite rock beam, MPa; M_{imax} is the maximum bending moment of the composite rock beam, taking the weighted average bending moment, kN·m.

According to the geometric damage theory, the damage of the material is caused by the deterioration of the mechanical properties caused by the micro-fractures and micro-pores inside the material, resulting in the decrease of effective bearing capacity. The relationship between the effective stress and the non-damage stress is expressed as follows:

$$\sigma' = \frac{\sigma}{1 - D} \quad (16)$$

where σ' is the effective stress, MPa; σ is the non-damage stress, MPa; D is the damage degree, which is usually obtained from the field measurement. In the absence of field measurement, the value can be obtained according to the complexity of the geological structure of the site. The structural development of coal-bearing strata is simple in the study area, and the D is calculated by 0.1.

The maximum effective tensile stress of composite rock beam failure considering the degree of damage:

$$\sigma'_{imax} = \left| \frac{6M_{imax}}{(1 - D)h_i^2} \right| \quad (17)$$

where σ'_{imax} is the maximum effective tensile stress, MPa.

According to the characteristics of coal mining and overburden failure, the volume of coal extracted from the working face is V_1 :

$$V_1 = Ml_1b_1 \quad (18)$$

where V_1 is the volume of mined coal, m^3 , b_1 is the width of the working face, m, M is the mining thickness.

After the failure of the composite rock beam, the volume of caving rock mass is V_2 :

$$V_2 = \frac{1}{2} \sum_{i=1}^n (l_i + l_{i+1})b_i h_i (k_p - 1) \quad (19)$$

where V_2 is the volume of rock mass, m^3 , b_i is the width of composite rock beam, m, k_p is the expansion coefficient of rock.

Iterative calculation, when the layer i rock beam satisfies Eq. 20, the fracture will occur and the process will continue to transmitted upward. When one of the conditions in Eq. 20 is not satisfied, the rock beam does not failure.

$$\begin{cases} V_1 \geq V_2 \\ \sigma'_{imax} \geq [\bar{\sigma}_i] \end{cases} \quad (20)$$

where $[\bar{\sigma}_i]$ is the average tensile strength of the composite rock beam, MPa.

The height of the overburden failure as follows:

$$H_{tf} = H_i - M \quad (21)$$

where H_{tf} is the height of overburden fracture, m, H_i is the distance between the rock beam of layer i and the coal floor, m, M is the mining thickness.

It can be seen that the height of mining-induced overburden fracture is mainly controlled by the mechanical properties of overburden, the volume of mined coal, and the expansion coefficient of rock. The weakly cemented strata, large mining thickness, and large mining width in the mining area of Western China are the main reasons for the ultra-high failure of overburden. The evolution process of the trapezoidal fracture model of overburden includes bending, cracking, and caving of the immediate roof, and then the failure of the basic roof successively, until the caving rock fills the whole mining space, and the overburden fracture stops developing upward. The trapezoidal fracture evolution is similar to Liu et al. (2022) trapezoidal collapse model, but the derivation process of the theoretical model is different. The model is derived based on the composite rock beam theory of foundation, which conforms to the failure rule of mining overburden. The introduced variable parameters are mainly the basic mechanical parameters of rock, which are easy to obtain. Considering the fracture failure characteristics of rock strata, and the concept of damage degree is introduced to improve the calculation accuracy. In addition, the iterative calculation process can be run with computer assistance, which greatly improves the computational efficiency.

3.2.2 Study Case

The 61,605 working face of LWGCM is 1156 m long and 255 m wide, with a mining thickness of 23 m. The buried depth of the coal seam is 421.3–512.7 m, and the roof strata of the coal are mainly mudstone, sandy mudstone, fine sandstone, medium sandstone, and coarse sandstone. The mine adopts fully mechanized caving technology. Taking the failure height of overburden in 61,605 working face mining as an example, the expansion coefficient (k_p) of mudstone, sandy mudstone, and sandstone are 1.10, 1.15, and 1.20, respectively, and the characteristic coefficient (λ) is 1.008. The fracture extension angle of the roof strata (δ) is 65° . The iterative calculation is realized by Matlab, and the end condition of the iteration is that the calculation results does not satisfies Eq. 20. Calculating the overburden failure height of 61,605 working face is 180 m.

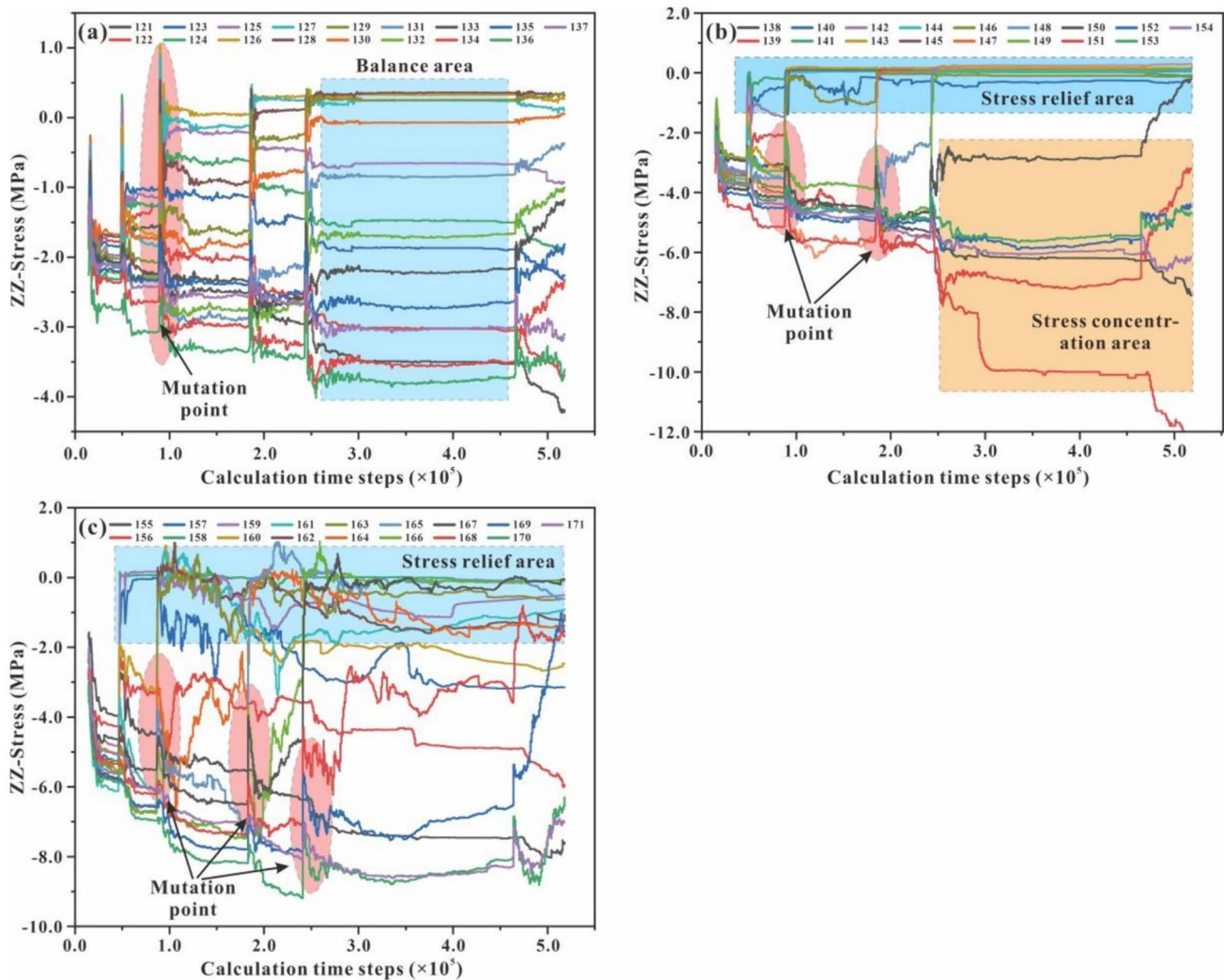


Fig. 13 Stress evolution of overburden in working face

3.3 Numerical Simulation Analysis

Figure 13 is the numerical simulation results of extra-thick coal mining in weakly cemented strata. When the working face is mined to 100 m, the basic roof is caved, as shown in Fig. 13a. There are 593 fractures, including 27 tensile fractures and 566 shear fractures, many water migration pathways began to form. When the working face is mined to 200 m, as shown in Fig. 13b. The overburden fracture gradually transmits upward, the failure range begins to develop in an approximately symmetrical “trapezoid”, and the height of overburden failure is 125 m. The fracture growth rate of the roof gradually increases, the fractures at the bottom of the trapezoidal zone are concentrated, and the groundwater migration channels begin to connect. Currently, 4059 fractures were generated, including 244 tensile fractures and 3815 shear fractures. When the working face is mined to 300 m, as shown in Fig. 13c, the height of the overburden

fracture is 182 m. There are 12,719 fractures were generated, including 827 tensile fractures and 11,892 shear fractures. The fractures at the bottom of the trapezoidal zone are gradually compressed, the middle and upper fractures are developed in large numbers, and the main fracture channels are gradually connected. When the working face is mined to 400 m, as shown in Fig. 13d. The maximum fracture height of overburden is 182 m, and the range of the trapezoidal failure zone is expanding. A total of 17,912 fractures were generated, including 1111 tensile fractures (6.2%) and 16,801 shear fractures (93.8%). The overburden has experienced extensive caving, and the height of the caving zone is about 55 m. The caving rock is gradually compacted at the bottom of the goaf, and the fracture channels are closed. The main fracture channels are distributed on both sides of the trapezoidal failure zone, forming the main groundwater migration channels. In different excavation stages, the fracture extension angle is not exactly the same, with an average of

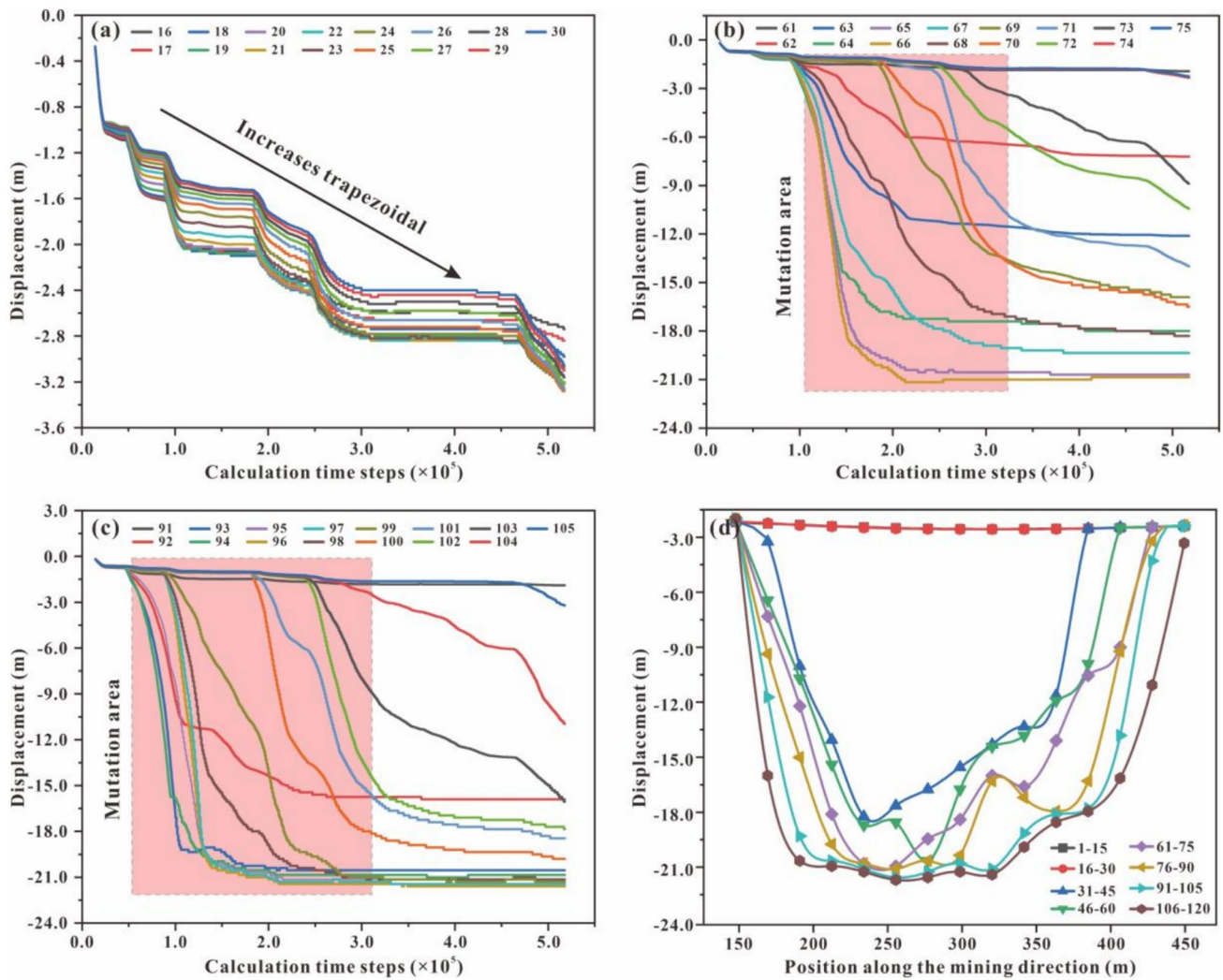


Fig. 14 Displacement evolution of overburden in working face

65°. The difference in the development of fracture extension angle when mining overburden fracture develops into a new stratum group.

The stress evolution of overburden during the mining process of the working face, as shown in Fig. 14. The monitoring points from 121 to 137 are located at the height of 350 m in the model, as shown in Fig. 14a, the stress curves of monitoring points regularly increase with the excavation steps, with the maximum stress reaching 4.0 MPa. It shows that the vertical stress of the working face propagates to the position of 350 m, but the disturbance is small, and the rock stratum is not failed. The monitoring points from 138 to 154 are located at the height of 275 m in the model. The stress curves of most monitoring points fluctuate regularly, as shown in Fig. 14b. When the model is mined to 300 m, the stress suddenly increased at 139 and 151 points, indicating that the rock stratum failure occurs. The rock stratum near the monitoring line is obviously affected

by mining, but only local failure occurs. It is inferred that the failure height of the overburden fracture is 185 m. The monitoring points from 155 to 171 are located at the height of 200 m in the model, as shown in Fig. 14c. When the working face is mined to 100 m, monitoring points stress gradually changes, and the stress curve fluctuates disorderly. With the excavation, the fluctuation of the stress curve is more obvious, indicating that the rock stratum near the monitoring line has a large range of failure.

At the height of 300 m, 210 m, and 150 m, the displacement monitoring curves are shown in Fig. 15a, b, and c. With the excavation of the working face, the displacement at the height of 300 m in the model increases slowly in a “step” shape, and the maximum displacement is 3.4 m. At the 210 m height of the model, the displacement increases rapidly from 150 m of the model, and the displacement of 66, 67, and 68 measuring points reaches 22.0 m. At the height of 150 m, the displacement of monitoring points are

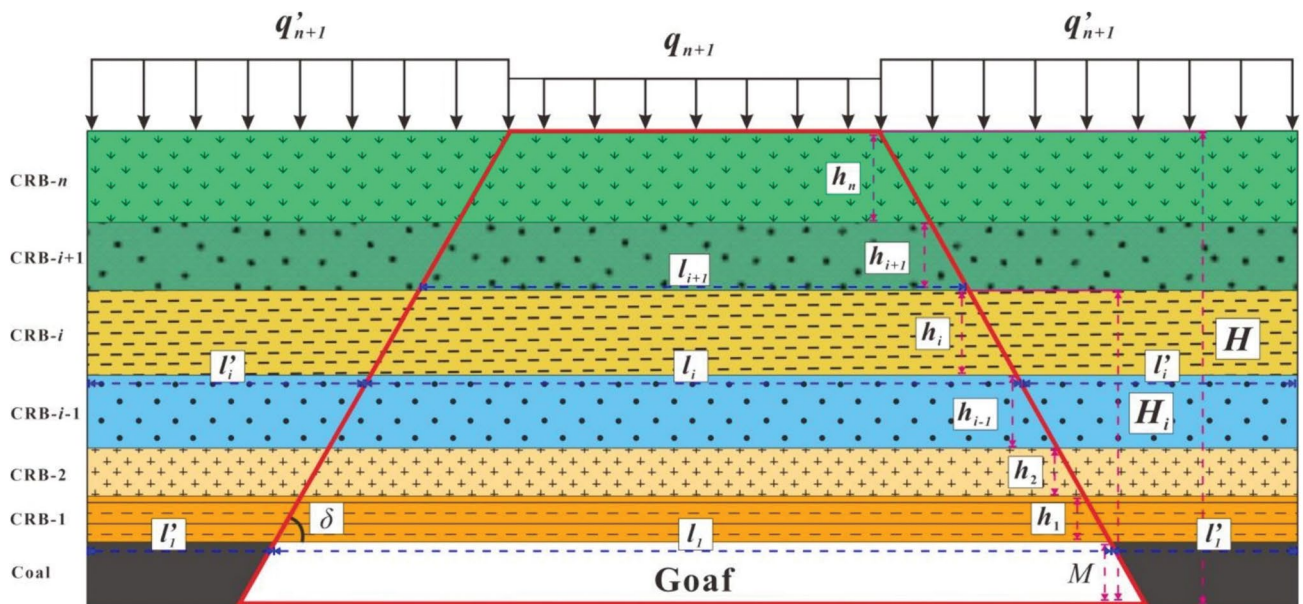


Fig. 15 Schematic diagram of trapezoidal fracture of mining overburden

generally large, and the position of the displacement mutation point moves forward, with the maximum displacement reaches 22.5 m. After the mining of the working face, the connections of all displacement monitoring points are shown in Fig. 15d. It can be seen that the displacement of measuring points decrease from the middle of the goaf to both sides, showing a “U” shape distribution. The farther the distance from the coal seam roof, the smaller the displacement of the measuring points from 1 to 30, which also shows that the model above 300 m is less affected by mining.

3.4 Microseismic Dynamic Monitoring Analysis

The monthly advancing lengths of the 61,605 working face in LWGCM are 107.5 m, 106 m, 102.4 m, 108 m, and 106 m, respectively. Figure 16 is the microseismic event distribution of vertical mining direction with advance of working face. The temporal and spatial distribution rule of microseismic events in surrounding rock during mining are revealed. A total of 29,036 microseismic events were monitored, including 5566 events in the roof, 22,038 events in the coal seam, 1432 events in the floor, and the total energy released was 9676.037 kJ. With the mining of the working face, the frequency and energy of microseismic events increases, revealing that the failure range of surrounding rock is expanding. The microseismic events are distributed in strips along the mining position to both sides. The density of microseismic events near the coal seam and the immediate roof position is high, and high-energy events occur frequently.

To better display the vertical distribution of microseismic events, it is superimposed with the geological section of the main transport. The failure range and profile of the roof along the transport section are shown in Fig. 17. The distribution of microseismic events is trapezoidal, with a height of 185 m. The density of microseismic events gradually decreases from the bottom to the top of the trapezoid. The density of microseismic events is larger in the range of 168 m above the coal roof, and there are few microseismic events in the range of 168 to 185 m. Therefore, it is inferred that the maximum development height of mining-induced fractures in overburden is 185 m, and fractures are more developed in the range of 168 m above the coal roof.

3.5 Comparison and Verification of the Height of Overburden Fracture

The overburden failure height of 61,605 working face in LWGCM are calculated by trapezoidal fracture model, empirical formula, PFC numerical simulation, and microseismic dynamic monitoring, and the results are shown in Table 5 shows the comparative analysis of overburden failure height. According to the rock mechanics test results of LWGCM, the compressive strength of the 6rd coal roof rock is 1.23–53.8 Mpa, and the tensile strength is 0.1–9.78 Mpa. Therefore, the overburden belong to the medium hard type. Equation 3 is used to calculate the overburden failure height is 62.5 m and the relative errors are – 65.7 and – 66.2%, which is seriously inconsistent with the actual. The calculation results of the trapezoidal fracture model are consistent with the numerical simulation and microseismic monitoring,

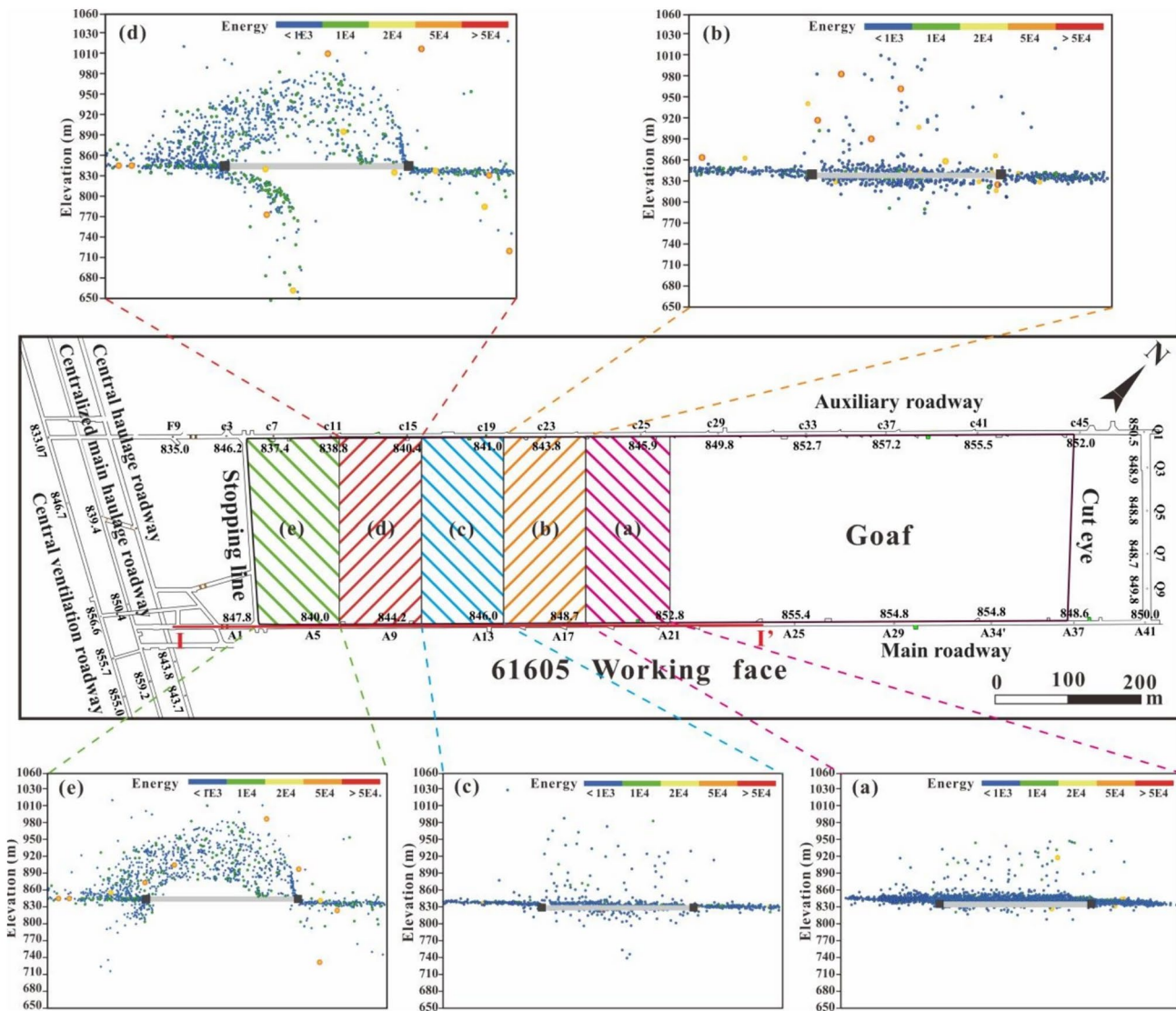


Fig. 16 Microseismic event distribution of vertical mining direction with advance of working face

the relative errors are -1.1% and -2.7% , indicating that the model calculation results are more accurate and reliable.

4 Conclusions

1. Based on the rock fracture propagation tests, the macroscopic and microscopic mechanical behaviors of rock strata under uniaxial compression is simulated and reconstructed. The failure process of weakly cemented rock is divided into four stages: No fracture stage, Micro-fracture propagation stage, Micro-fracture accelerated propagation stage, and Post-peak fractures coalescence failure stage. Fractures develop rapidly after the peak point, accounting for about 94% of the whole failure process.
2. Based on the optimized rock mechanics parameters, a numerical model of extra-thick coal mining is constructed. The overburden fracture in mining face is trapezoidal evolution, including shear fractures (93.8%) and tensile fractures (6.2%). Mining-induced fractures are mainly distributed on both sides of the trapezoidal failure zone, forming the main groundwater migration channels.
3. According to the elastic foundation beam and fracture damage theory, the calculation method of overburden failure height in extra-thick coal mining is derived. The model predicts that the overburden failure height of 61,605 working face in LWGCM is 180 m, and the relative errors are -1.1% and -2.7% .
4. The microseismic monitoring results show that a total of 29,036 microseismic events occur during the min-

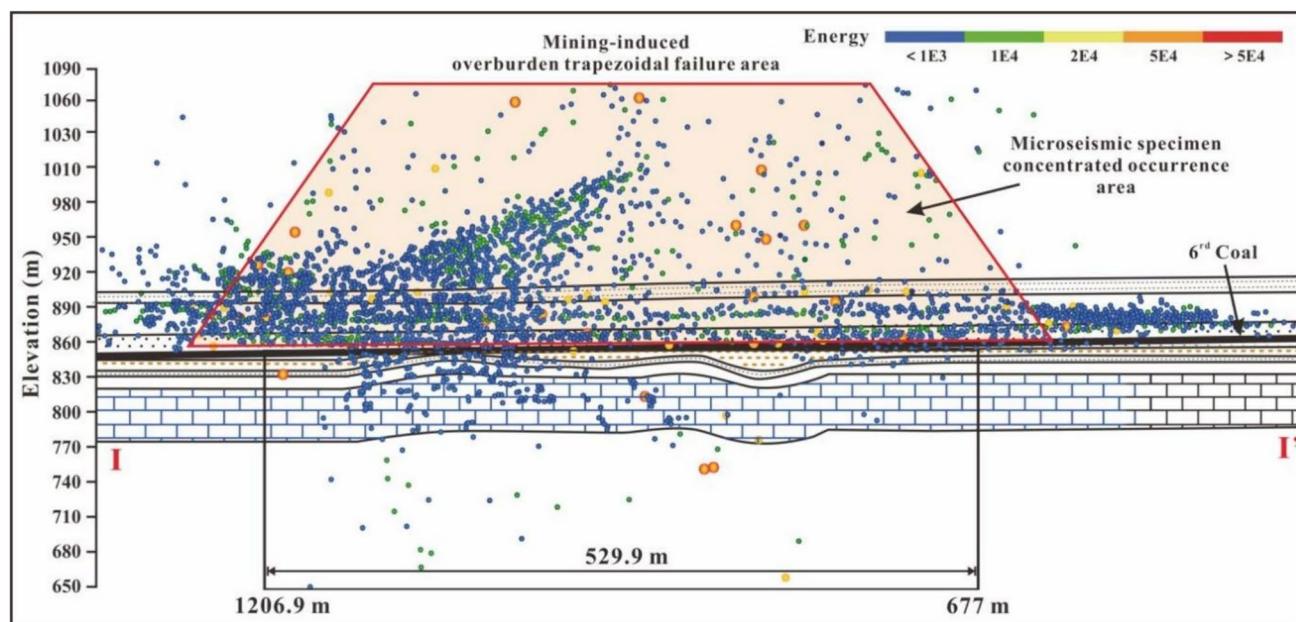


Fig. 17 Microseismic event distribution of section I–I' along the main roadway

Table 5 Comparison of overburden failure height

	Overburden failure height (m)	Comparison with H_{PFC}		Comparison with H_{mm}	
		Absolute error (m)	Relative error (%)	Absolute error (m)	Relative error (%)
H_{tf}	180	– 2.0	– 1.1	– 5.0	– 2.7
H_{mh}	62.5	– 119.5	– 65.7	– 132.5	– 66.2
H_{PFC}	182	0	0	– 3.0	– 1.6
H_{mm}	185	3.0	1.6	0	0

ing process of the working face, releasing energy 9676.037 kJ. The roof microseismic events are trapezoidal distribution with a maximum development height of 185 m, which further verifies the accuracy of the trapezoidal fracture model and PFC simulation results.

Acknowledgements This work was supported by the National Key R&D Program of China under Grant No. 2017YFC0804100, the National Natural Science Foundation of Shandong Province under Grant No. ZR2019MD013.

Author contributions Fangying Dong: Formal analysis, Writing—original draft; Huiyong Yin: Writing—review and editing, Supervision, Funding acquisition; Hongxu Ren: Methodology, Writing—original draft, Project administration; Wenju Cheng: Investigation, Visualization; Shuzhen Tai: Methodology, Software; Tianyu Miao: Data curation, Software; Yian Zhang: Investigation; Bin Wu: Formal analysis, Methodology.

Funding The National Key R&D Program of China, 2017YFC0804100, Huiyong Yin, the National Natural Science Foundation of Shandong Province, ZR2019MD013, Huiyong Yin.

Data availability The authors declare that data will be made available on request.

Declarations

Conflict of interest The authors declare that they have no known competing financial interests or personal relationships that could have appeared to influence the work reported in this paper.

References

- Banerjee L, Chawla S, Dash SK (2020) Application of geocell reinforced coal mine overburden waste as subballast in railway tracks on weak subgrade. *Constr Build Mater* 265:120774. <https://doi.org/10.1016/j.conbuildmat.2020.120774>
- Blixt K, Hallberg H (2022) Evaluation of grain boundary energy, structure and stiffness from phase field crystal simulations.

- Model Simul Mater Sc 30(1):014002. <https://doi.org/10.1088/1361-651X/ac3ca1>
- Cai YF, Li XJ, Xiao W, Zhang WK (2020) Simulation of mining-induced ground damage using orthogonal experiments to determine key parameters of super-large coalface: a case study in Shendong Coalfield in China. *Appl Sci* 10(7):2258. <https://doi.org/10.3390/app10072258>
- Chauhan M, Dwivedi S, Mishra P, Ragulskis M, Burdzik R, Ranjan V (2023) Exponential functionally graded plates resting on Winkler-Pasternak foundation: free vibration analysis by dynamic stiffness method. *Arch Appl Mech* 93(6):2483–2509. <https://doi.org/10.1007/s00419-023-02392-6>
- Cheng G, Xu WT, Shi B, Wu JH, Sun BY, Zhu HH (2022) Experimental study on the deformation and failure mechanism of overburden rock during coal mining using a comprehensive intelligent sensing method. *J Rock Mech Geotech* 14(05):1626–1641. <https://doi.org/10.1016/J.JRMGE.2022.07.016>
- Coal Industry Bureau of China (2000) Coal mining regulations and coal pillar design affected by building, water bodies, railways and main roadway. China Coal Industry Publishing House, Beijing
- Deng GD, Xie HP, Gao MZ, Xie J, Li C, He ZQ (2022) Fracture mechanisms of competent overburden under high stress conditions: a case study. *Rock Mech Rock Eng* 56(3):1759–1777. <https://doi.org/10.1007/s00603-022-03169-z>
- Dong FY, Yin HY, Cheng WJ, Li YJ, Qiu M, Zhang C, Tang RQ, Xu GL, Zhang LF (2022a) Study on water inrush pattern of ordovician limestone in North China Coalfield based on hydrochemical characteristics and evolution processes: a case study in Binhu and Wangchao Coal Mine of Shandong Province, China. *J Clean Prod* 380:134954. <https://doi.org/10.1016/J.JCLEPRO.2022.134954>
- Dong S, Liu Z, Wang H (2022b) Research status and prospect on the mechanism of dynamics and inrush at weakly cemented strata in working face with thick bedrock. *J China Coal Soc* 47(01):274–285
- Dong FY, Yin HY, Cheng WJ, Zhang C, Zhang DY, Ding HX, Lu C, Wang Y (2024) Quantitative prediction model and prewarning system of water yield capacity (WYC) from coal seam roof based on deep learning and joint advanced detection. *Energy* 290:130200. <https://doi.org/10.1016/J.ENERGY.2023.130200>
- Feng G, Kang Y, Chen F, Liu YW, Wang XC (2018) The influence of temperatures on mixed-mode (I + II) and mode-II fracture toughness of sandstone. *Eng Fract Mech* 189:51–63. <https://doi.org/10.1016/j.engfracmech.2017.07.007>
- Feng G, Wang XC, Kang Y, Zhang ZT (2020) Effect of thermal cycling-dependent cracks on physical and mechanical properties of granite for enhanced geothermal system. *Int J Rock Mech Min* 134:104476
- Hasenfuß G, Johnson K, Su D (1998) A hydrogeomechanical study of overburden aquifer response to longwall mining. In: Proceedings of 7th international conference on ground control in mining. Morgantown, WV
- Huang Y, Xia X (2021) Calibration method of mesoscopic parameters for parallel bonding model of sandstone particle flow. *J China Three Gorges Univ (Nat Sci)* 43(04):7–12. <https://doi.org/10.13393/j.cnki.issn.1672-948x.2021.04.002>
- Kang YH, Huang FC (2001) Xi JD (2001) Overburden rock failure law of fully mechanized repeated mining. *Coal Sci Tech* 01:22–24+0
- Kuva J, Siitari-Kauppi M, Lindberg A, Aaltonen I, Turpeinen T, Mylly M, Timonen J (2012) Microstructure, porosity and mineralogy around fractures in Olkiluoto bedrock. *Eng Geol* 139(14):28–37. <https://doi.org/10.1016/j.enggeo.2012.04.008>
- Li XB, Peng DX, Feng F, Li XS (2019) Stability analysis of horizontal insulating pillar in deep mining from caving to filling method on the basis of refined plate theory. *J China Univ Min Tech* 48(03):484–494. <https://doi.org/10.13247/j.cnki.jcumt.001003>
- Li RR, Zhang LQ, Zhou J, Han ZH, Pan ZJ, Schuettrumpf H (2023) Investigation on permeability anisotropy in unconsolidated hydrate-bearing sediments based on pore-scale numerical simulation: effect of mineral particle shape and pore-filling. *Energy* 267:126456. <https://doi.org/10.1016/j.energy.2022.126456>
- Liu S, Yang K, Zhang T, Tang CA (2020) Rib spalling 3D model for soft coal seam faces with large mining height in protective seam mining: theoretical and numerical analyses. *Geofluids* 2020:8828844. <https://doi.org/10.1155/2020/8828844>
- Liu XS, Fan DY, Tan YL, Ning JG, Song SL, Wang HL, Li XB (2021) New detecting method on the connecting fractured zone above the coal face and a case study. *Rock Mech Rock Eng* 54(8):4379–4391. <https://doi.org/10.1007/s00603-021-02487-y>
- Liu TH, Xu DJ, Shi LQ, Qu LY, Ji KM (2022) Trapezoidal collapse model to calculate the height of the overburden collapse zone in coal seam mining: an example from Guo' Jiahe Coal Mine Western China. *Energy*. <https://doi.org/10.1016/J.ENERGY.2022.124609>
- Liu X, Miao L, Fu Y, Yuan W, Wang Z (2018) Quantitative determination approach of rock micro tensile strength based on particle flow code. Proceedings of Geoshanghai 2018 International Conference: Fundamentals of soil behaviours. https://doi.org/10.1007/978-981-13-0125-4_105
- Mekhtiev AD, Sarsikeev EJ, Neshina AA, Musagazhinov M (2022) A quasi-distributed fiber-optical monitoring system for movement of roof strata in mines. *J Min Sci* 58(2):338–346. <https://doi.org/10.1134/S1062739122020168>
- Meng XJ, Zhang GC, Li Y, Chen LJ, Wang C, Zhao RB, Tao GZ, Wang D, Zhou GL, Chen M, Luan HJ (2023) Migration evolution laws of overburden structure with deep-lying thick surface soil and disaster mechanism induced by high stress mutation. *J China Coal Soc* 48(05):1919–1931
- Miao LT, Xia YC, Lv TT, Sun XY, Du RJ (2018) Study on coal seam occurrence features and control mechanism in Linyou Area of Ordos Basin. *Coal Sci Tech* 46(11):163–171. <https://doi.org/10.13199/j.cnki.cst.2018.11.026>
- Queiroz HM, Ferreira AD, Ruiz F, Bovi RC, Deng YJ, De SJ, Otero XL, Bernardino AF, Cooper M, Ferreira TO (2022) Early pedogenesis of anthropogenic soils produced by the world's largest mining disaster, the “Fundão” dam collapse, in southeast Brazil. *CATENA* 219:106625. <https://doi.org/10.1016/J.CATENA.2022.106625>
- Redondo-Vega JM, Gómez-Villar A, Santos-González J, González-Gutiérrez R, Álvarez-Martínez J (2017) Changes in land use due to mining in the north-western mountains of Spain during the previous 50 years. *CATENA* 149:844–856. <https://doi.org/10.1016/j.catena.2016.03.017>
- Rezaei M, Hossaini MF, Majdi A (2015) A time-independent energy model to determine the height of distressed zone above the mined panel in longwall coal mining. *Tunn Undergr Sp Tech* 47:81–92. <https://doi.org/10.1016/j.tust.2015.01.001>
- Ríos-Bayona F, Johansson F, Mas-Ivars D, Sánchez-Juncal A, Bolin A (2022) Using PFC^{2D} to simulate the shear behaviour of joints in hard crystalline rock. *B Eng Geol Environ* 81(09):381. <https://doi.org/10.1007/S10064-022-02885-8>
- Satake K, Okada K, Muramatsu M (2021) Phase-field crack analysis using estimated transition zone of crack by molecular dynamics simulation. *Aip Adv* 11(6):065206. <https://doi.org/10.1063/5.0054236>
- Scott DA, Lessel AM, Williams BA, Horner WM, Ranade R (2023) Fracture process zone characterizations of multi-scale fiber reinforced cementitious composites. *Constr Build Mater* 408:133713. <https://doi.org/10.1016/j.conbuildmat.2023.133713>
- Stricker K, Schimschal S, Mueller B, Wessling S, Bender F, Kohl T (2023) Importance of drilling-related processes on the origin of

- borehole breakouts-Insights from LWD observations. *Geomech Energy Envir* 34:100463. <https://doi.org/10.1016/j.gete.2023.100463>
- Su BY, Yue JH (2017) Research of the electrical anisotropic characteristics of water-conducting fractured zones in coal seams. *Appl Geophys* 14(2):216–224. <https://doi.org/10.1007/s11770-017-0620-2>
- Sun YJ, Zuo JP, Karakus M, Wen JH (2019) A novel method for predicting movement and damage of overburden caused by shallow coal mining. *Rock Mech Rock Eng* 53(4):1545–1563. <https://doi.org/10.1007/s00603-019-01988-1>
- Wang SR, Wu XG, Zhao YH, Hagan P, Cao C (2019) Evolution characteristics of composite pressure-arch in thin bedrock of overlying strata during shallow coal mining. *Int J Appl Mech* 11(3):1950030. <https://doi.org/10.1142/S1758825119500303>
- Wang CG, Wang SH, Chen GQ, Yu PC, Peng XY (2021a) Implementation of a J-integral based maximum circumferential tensile stress theory in DDA for simulating crack propagation. *Eng Fract Mech* 246:107621. <https://doi.org/10.1016/j.engfracmech.2021.107621>
- Wang ZK, Li WP, Wang QQ, Hu YB, Du JF (2021b) Monitoring the dynamic response of the overlying rock-soil composite structure to underground mining using BOTDR and FBG sensing technologies. *Rock Mech Rock Eng* 54(9):5095–5116. <https://doi.org/10.1007/s00603-021-02530-y>
- Wilkins AH, Strange A, Duan Y, Luo X (2020) Identifying micro-seismic events in a mining scenario using a convolutional neural network. *Comput Geosci-UK* 137:104418–104418. <https://doi.org/10.1016/j.cageo.2020.104418>
- Yang ZP, Zhao Q, Liu XR, Yin ZM, Zhao YL, Li XY (2022) Experimental study on the movement and failure characteristics of karst mountain with deep and large fissures induced by coal seam mining. *Rock Mech Rock Eng* 55(8):4839–4867. <https://doi.org/10.1007/s00603-022-02910-y>
- Yin HY, Zhou WF, LaMoreaux JW (2018) Water inrush conceptual site models for coal mines of China. *Environ Earth Sci* 77(22):1–7. <https://doi.org/10.1007/s12665-018-7920-6>
- Yu B, Zhao J, Kuang TJ, Meng XB (2015) In situ investigations into overburden failures of a super-thick coal seam for longwall top coal caving. *Int J Rock Mech Min* 78:155–162. <https://doi.org/10.1016/j.ijrmms.2015.05.009>
- Zhang Z, Xie HP, Zhang R, Gao MZ, Ai T, Zha E (2020) Size and spatial fractal distributions of coal fracture networks under different mining-induced stress conditions. *Int J Rock Mech Min* 132:104364. <https://doi.org/10.1016/j.ijrmms.2020.104364>
- Zhang XQ, Hu BL, Zou JX, Liu CD, Ji YF (2021a) Quantitative characterization of overburden rock development pattern in the goaf at different key stratum locations based on DEM. *Adv Civ Eng* 2021:8011350. <https://doi.org/10.1155/2021/8011350>
- Zhang YS, Niu K, Du WZ, Zhang J, Wang HW, Zhang J (2021b) A method to identify coal spontaneous combustion-prone regions based on goaf flow field under dynamic porosity. *Fuel* 288:119690. <https://doi.org/10.1016/j.fuel.2020.119690>
- Zhang JM, Meng FL, Wu HW, Zhao F, Xue JK, Wang Y, Luo AK, Huang H (2022) Study on development law of water conducting fracture zone in coal seam mining under burnt rock aquifer. *Safety Coal Mines*. 53(08):180–186. <https://doi.org/10.13347/j.cnki.mkaq.2022.08.029>
- Zhang C, Bai QS, Han PH (2023) A review of water rock interaction in underground coal mining: problems and analysis. *B Eng Geol Environ* 82(5):157. <https://doi.org/10.1007/s10064-023-03142-2>
- Zhu ZG, Li YF, Chen T, Ruan XY, Wang GW (2023) Study on breaking law of hard thick layer roof and surrounding rock control. *Coal Technolo* 42(06):25–29. <https://doi.org/10.13301/j.cnki.ct.2023.06.006>

Publisher's Note Springer Nature remains neutral with regard to jurisdictional claims in published maps and institutional affiliations.

Springer Nature or its licensor (e.g. a society or other partner) holds exclusive rights to this article under a publishing agreement with the author(s) or other rightsholder(s); author self-archiving of the accepted manuscript version of this article is solely governed by the terms of such publishing agreement and applicable law.